

Mixed-grid and staggered-grid finite-difference methods for frequency-domain acoustic wave modelling

Bernhard Hustedt, Stéphane Operto and Jean Virieux

UMR Géosciences Azur, CNRS-UNSA-UPMC, France. E-mails: hustedt@geoazur.unice.fr; operto@obs-vm.fr; virieux@geoazur.unice.fr

Accepted 2004 March 12. Received 2004 February 10; in original form 2002 June 21

SUMMARY

We compare different finite-difference schemes for two-dimensional (2-D) acoustic frequency-domain forward modelling. The schemes are based on staggered-grid stencils of various accuracy and grid rotation strategies to discretize the derivatives of the wave equation. A combination of two $\mathcal{O}(\Delta x^2)$ staggered-grid stencils on the classical Cartesian coordinate system and the 45° rotated grid is the basis of the so-called mixed-grid stencil. This method is compared with a parsimonious staggered-grid method based on a fourth-order approximation of the first derivative operator. Averaging of the mass acceleration can be incorporated in the two stencils. Sponge-like perfectly matched layer absorbing boundary conditions are also examined for each stencil and shown to be effective.

The deduced numerical stencils are examined for both the wavelength content and azimuthal variation. The accuracy of the fourth-order staggered-grid stencil is slightly superior in terms of phase velocity dispersion to that of the mixed-grid stencil when averaging of the mass acceleration term is applied to the staggered-grid stencil.

For fourth-order derivative approximations, the classical staggered-grid geometry leads to a stencil that incorporates 13 grid nodes. The mixed-grid approach combines only nine grid nodes. In both cases, wavefield solutions are computed using a direct matrix solver based on an optimized multifrontal method. For this 2-D geometry, the staggered-grid strategy is significantly less efficient in terms of memory and CPU time requirements because of the enlarged bandwidth of the impedance matrix and increased number of coefficients in the discrete stencil.

Therefore, the mixed-grid approach should be suggested as the routine scheme for 2-D acoustic wave propagation modelling in the frequency domain.

Key words: derivative stencils, finite-difference methods, frequency-domain wave modelling, seismic wave propagation.

1 INTRODUCTION

Modelling seismic wave propagation is essential for understanding complex wave phenomena in a realistic heterogeneous medium. Numerical results from finite-difference (FD) modelling are particularly useful since they provide the complete wavefield response. Frequency-domain forward modelling is of special interest for multisource experiments, such as tomographic experiments, because of its computational efficiency (Pratt & Worthington 1990; Štekl & Pratt 1998). Moreover, realistic rheology is easily incorporated into the modelling scheme by introducing complex velocities. The key step in frequency-domain finite-difference (FDFD) modelling that controls computational efficiency is the numerical inversion of a massive matrix equation. The matrix structure depends on the spatial derivative approximations. We shall discuss what the useful features of this matrix are for wave modelling accuracy and for computational efficiency.

Elastodynamic finite-difference time-domain (FDTD) techniques moved from second-order approximations of spatial derivatives (Madariaga 1976; Virieux 1984, 1986) to higher-order approximations (Dablain 1986; Levander 1988) using staggered-grid stencils with a good trade-off between modelling accuracy and computational efficiency for the fourth-order spatial approach. Constructions of FDFD schemes have followed a similar path. Pratt & Worthington (1990) and Pratt (1990) have applied second-order spatial derivative approximations in two dimensions to the acoustic and elastic wave equations using centred finite-difference (FD) discretizations on a single grid. This leads to five-point and nine-point stencils for the acoustic and elastic wave equations respectively. Their scheme required 10 gridpoints per shortest wavelength for accurate modelling. Jo *et al.* (1996) reduced the number of gridpoints per shortest wavelength to about four by including additional surrounding gridpoints for the derivative approximations in the acoustic wave equation. The approach consists of linearly combining

two discretizations of the second derivative operator on the classical Cartesian coordinate system and the 45° rotated system. Combination of the two discretizations mitigates the anisotropy of the stencil but increases its numerical dispersion. Additional weighted averaging of the mass acceleration term over the gridpoints of the FD stencil gives a compact stencil with both optimal anisotropy and dispersion properties. The weight coefficients which are required to mix the two different derivative stencils and average the acceleration term are derived by an optimization technique that minimizes the phase velocity dispersion. The approach of Jo *et al.* (1996) will be referred to in the following as the mixed-grid method.

The mixed-grid approach was extended to the elastic wave equation by Štekl & Pratt (1998). In the elastic case, the approach is more complicated since vectorial fields must be manipulated. Moreover, the weight coefficients depend on the Poisson ratio. In the fluid case, the mixed-grid stencil must be adapted such that only the discretization on the rotated frame is used (Štekl & Pratt 1998).

A second extension of the mixed-grid method was developed by Shin & Sohn (1998). They applied a 25-point stencil to the acoustic wave equation. Four directions (0° , 26.6° , 45° and 63.4°) were considered to discretize the Laplacian. The number of gridpoints per shortest wavelength was reduced to two and a half instead of four for the nine-point mixed-grid stencil. For these discretization rules, the bandwidth of the impedance matrix remains the same but the number of core memory elements is reduced by a factor of four when using the 25-point stencil (Shin & Sohn 1998). One drawback of the 25-point stencil may be that structures whose size is smaller than one wavelength and complex topographies cannot be properly discretized when using two and a half points per wavelength. Moreover, the source implementation on a coarse grid may lead to some inaccuracies.

While time-domain approaches rely strongly on the staggered-grid structure, the frequency-domain formulations were developed on non-staggered-grid strategies. We shall analyse why different strategies have been developed. In order to do so, we focus our attention on the acoustic wave equation.

In the following, we first present a parsimonious second-order staggered-grid formulation of the acoustic wave equation in the frequency domain following Luo & Schuster (1990). The acoustic wave equation is formulated as a first-order hyperbolic system (Virieux 1984) involving fields as the pressure and the particle velocities. This system is discretized using second-order staggered-grid stencils. Then, particle velocities are eliminated from the coupled first-order equations. Elimination of particle velocities leads to the so-called parsimonious second-order staggered-grid formulation. This parsimonious formulation only involves the pressure field in the second-order wave equation.

We shall show the identity between the parsimonious second-order staggered-grid stencil and the five-point stencil originally developed by Pratt & Worthington (1990). We also develop the second-order staggered-grid stencil on the 45° rotated coordinate system following the same parsimonious elimination procedure. This rotated stencil construction was recently proposed by Saenger *et al.* (2000) for time-domain modelling of the elastic wave equation.

The two second-order derivations provide a general framework within which to discretize the frequency-domain second-order acoustic wave equation based on a parsimonious staggered-grid approach. A sponge-like perfectly matched layer (PML) absorbing boundary condition (Berenger 1994) is also developed for both stencils.

In Section 3 we present two improved discretizations of the frequency-domain wave equation. The first relies on the approach of Jo *et al.* (1996). We clarify the close connection between the staggered-grid and the mixed-grid method: the mixed-grid method combines two second-order staggered-grid stencils to mimic a fourth-order accurate FD stencil. We also provide a qualitative interpretation to justify why the acceleration averaging in the mixed-grid method is a key component of the method. The second discretization extends to fourth-order accuracy the parsimonious second-order staggered-grid method. This discretization leads to a 13-point stencil.

In Section 4 the dispersion properties of the mixed-grid and fourth-order staggered-grid stencils are compared through a classical harmonic analysis. We show that the accuracy of the fourth-order staggered-grid stencil is slightly better than the mixed-grid stencil when averaging of the mass acceleration term is applied to the staggered-grid stencil.

In Section 5 we compare the structure of the impedance matrices of the two stencils. The CPU and RAM performances of the mixed-grid method are expected to be significantly superior to those of the fourth-order staggered-grid method. This results from the enlargement of the matrix bandwidth when using the 13-point stencil associated with the fourth-order staggered-grid method. Due to their compactness, the mixed-grid stencils appear to be optimal in terms of CPU and RAM performances, as has already been demonstrated by Štekl & Pratt (1998).

In Section 6 we present two numerical examples to quantify the accuracy and CPU performances of the mixed-grid stencil and the fourth-order staggered-grid stencil.

2 THE SECOND-ORDER FINITE-DIFFERENCE DISCRETIZATION

2.1 The first staggered-grid strategy

In seismology the staggered-grid strategy has so far been developed mainly in the time domain (Madariaga 1976; Virieux 1984, 1986). The staggered leap-frog structure of the numerical grid guarantees accurate derivative estimations and good performance for wave propagation dispersion.

We formulate the acoustic wave equation as a first-order hyperbolic system (Virieux 1984) using physical quantities such as the pressure and the particle velocity. Sponge-like PML at the edges of the necessary limited numerical model are implemented to absorb energy (Berenger

1994). The system of hyperbolic equations is given by:

$$\begin{aligned} \frac{\partial P_x(x, z, t)}{\partial t} + \gamma_x(x)P_x(x, z, t) &= K(x, z)\frac{\partial Q(x, z, t)}{\partial x} + S(x, z, t) \\ \frac{\partial P_z(x, z, t)}{\partial t} + \gamma_z(z)P_z(x, z, t) &= K(x, z)\frac{\partial R(x, z, t)}{\partial z} \\ \frac{\partial Q(x, z, t)}{\partial t} + \gamma_x(x)Q(x, z, t) &= b(x, z)\left(\frac{\partial P_x(x, z, t)}{\partial x} + \frac{\partial P_z(x, z, t)}{\partial x}\right) \\ \frac{\partial R(x, z, t)}{\partial t} + \gamma_z(z)R(x, z, t) &= b(x, z)\left(\frac{\partial P_x(x, z, t)}{\partial z} + \frac{\partial P_z(x, z, t)}{\partial z}\right) \end{aligned} \quad (1)$$

where wavefields $Q(x, z, t)$ and $R(x, z, t)$ are components of the particle velocity vector on the Cartesian grid while the pressure $P(x, z, t)$ is split into two components, $P_x(x, z, t)$ and $P_z(x, z, t)$, for separation of horizontal and vertical derivatives. The pressure wavefield is deduced through the simple addition of the two unphysical acoustic fields P_x and P_z , $P(x, z, t) = P_x(x, z, t) + P_z(x, z, t)$. The two unphysical acoustic fields P_x and P_z are used to account for the PML absorbing boundary conditions (see Zhang & Ballmann 1997; Operto *et al.* 2002, for application of PML boundary conditions to the *SH* and *P-SV* wave equations). $S(x, z, t)$ is the pressure source term applied to the sum of the first two equations of eqns (1) outside the PML layers (in that case, the γ functions are zero):

$$\frac{\partial P(x, z, t)}{\partial t} = K(x, z)\frac{\partial Q(x, z, t)}{\partial x} + K(x, z)\frac{\partial R(x, z, t)}{\partial z} + S(x, z, t). \quad (2)$$

Since the pressure source term is an additive term, it can be equivalently applied either to the first or second equation of system (1).

The inverse of the density is denoted by the buoyancy $b(x, z)$. If the bulk modulus $K(x, z)$ grid defines the reference grid (i.e. the grid input in the numerical code), the density (or the buoyancy) needs to be interpolated between gridpoints horizontally and vertically (see the classical geometry in Fig. 1). We used harmonic averaging of the density to compute such an interpolation (Kelly *et al.* 1976; Graves 1996).

The 1-D functions γ_x and γ_z define the PML damping behaviour in the PML layers surrounding the model on all four sides. These functions differ from zero only inside the PML layers. In the PML layers, we used $\gamma(x) = c_{\text{PML}} \cos(\frac{\pi}{2} \frac{x}{L})$ where L denotes the width of the PML layer and x is a local coordinate in the PML layer whose origin is located at the outer edges of the model. The scalar c_{PML} is defined by trial and error depending on the width of the PML layer (i.e. several values of c_{PML} are tested for representative PML widths; the best value is the one for which the reflections coming from the edges of the model have the smallest amplitude).

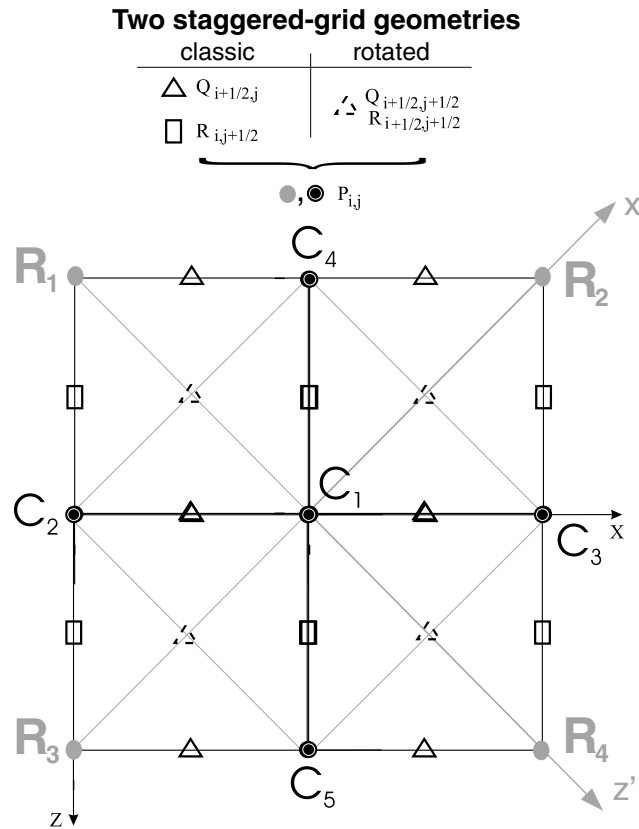


Figure 1. Illustration of different staggered finite-difference grids. Besides the pressure field, staggered-grid formulations of the acoustic wave equation introduce two additional variables, Q and R . The first classical discretization strategy gives different positions for these variables while the second alternative rotation strategy requires these variables to be located at the same grid node position.

We transform the system of equations to the Fourier domain and introduce the new functions $\xi_x(x) = 1 + i\gamma_x(x)/\omega$ and $\xi_z(z) = 1 + i\gamma_z(z)/\omega$ to simplify the equations:

$$\begin{aligned} \frac{-i\omega\xi_x(x)}{K(x,z)} P_x(x,z,\omega) &= \frac{\partial Q(x,z,\omega)}{\partial x} + S(x,z,\omega) \\ \frac{-i\omega\xi_z(z)}{K(x,z)} P_z(x,z,\omega) &= \frac{\partial R(x,z,\omega)}{\partial z} \\ -i\omega Q(x,z,\omega) &= \frac{b(x,z)}{\xi_x(x)} \frac{\partial P(x,z,\omega)}{\partial x} \\ -i\omega R(x,z,\omega) &= \frac{b(x,z)}{\xi_z(z)} \frac{\partial P(x,z,\omega)}{\partial z}. \end{aligned} \quad (3)$$

We discretize the hyperbolic equation system (3) using second-order centred finite differences of partial derivatives:

$$\begin{aligned} \left[\frac{\partial Q}{\partial x} \right]_{i,j} &\approx \frac{1}{\Delta} (Q_{i+1/2,j} - Q_{i-1/2,j}) \\ \left[\frac{\partial R}{\partial z} \right]_{i,j} &\approx \frac{1}{\Delta} (R_{i,j+1/2} - R_{i,j-1/2}), \end{aligned} \quad (4)$$

where Δ is the mesh spacing in the uniform grid. We obtain the following discrete system of equations:

$$\begin{aligned} \frac{-i\omega\xi_{xi}}{K_{i,j}} P_{x_{i,j}} &= \frac{1}{\Delta} (Q_{i+1/2,j} - Q_{i-1/2,j}) + S_{i,j} \\ \frac{-i\omega\xi_{zi}}{K_{i,j}} P_{z_{i,j}} &= \frac{1}{\Delta} (R_{i,j+1/2} - R_{i,j-1/2}) \\ -i\omega Q_{i+1/2} &= \frac{b_{i+1/2,j}}{\xi_{xi+1/2}} \frac{1}{\Delta} (P_{i+1,j} - P_{i,j}) \\ -i\omega R_{j+1/2} &= \frac{b_{i,j+1/2}}{\xi_{zj+1/2}} \frac{1}{\Delta} (P_{i,j+1} - P_{i,j}) \\ -i\omega Q_{i-1/2} &= \frac{b_{i-1/2,j}}{\xi_{xi-1/2}} \frac{1}{\Delta} (P_{i,j} - P_{i-1,j}) \\ -i\omega R_{j-1/2} &= \frac{b_{i,j-1/2}}{\xi_{zj-1/2}} \frac{1}{\Delta} (P_{i,j} - P_{i,j-1}), \end{aligned} \quad (5)$$

where we have introduced the averaged coefficients $b_{i+1/2,j} = \frac{1}{2}(b_{i+1,j} + b_{i,j})$, and $\xi_{xi+1/2} = \frac{1}{2}(\xi_{xi+1} + \xi_{xi})$.

We eliminate the additional equations depending on Q and R by re-injecting them into the first two equations that depend on P_x and P_z only, and obtain the compact system of equations:

$$\begin{aligned} \frac{-i\omega\xi_{xi}}{K_{i,j}} P_{x_{i,j}} &= \frac{1}{\Delta} \left(-\frac{1}{i\omega} \frac{b_{i+1/2,j}}{\xi_{xi+1/2}} \frac{1}{\Delta} (P_{i+1,j} - P_{i,j}) + \frac{1}{i\omega} \frac{b_{i-1/2,j}}{\xi_{xi-1/2}} \frac{1}{\Delta} (P_{i,j} - P_{i-1,j}) \right) + S_{i,j} \\ \frac{-i\omega\xi_{zi}}{K_{i,j}} P_{z_{i,j}} &= \frac{1}{\Delta} \left(-\frac{1}{i\omega} \frac{b_{i,j+1/2}}{\xi_{zj+1/2}} \frac{1}{\Delta} (P_{i,j+1} - P_{i,j}) + \frac{1}{i\omega} \frac{b_{i,j-1/2}}{\xi_{zj-1/2}} \frac{1}{\Delta} (P_{i,j} - P_{i,j-1}) \right). \end{aligned} \quad (6)$$

The procedure for eliminating the Q and R fields in the discretized equations of system (6) defines the so-called parsimonious approach (Luo & Schuster 1990).

We sum the two unphysical wavefields, P_x and P_z , and get the second-order finite-difference equation with PML absorbing boundary conditions for the pressure wavefield P :

$$\begin{aligned} \frac{-\omega^2}{K_{i,j}} P_{i,j} &= \frac{1}{\xi_{xi}} \frac{1}{\Delta^2} \left(\frac{b_{i+1/2,j}}{\xi_{xi+1/2}} (P_{i+1,j} - P_{i,j}) - \frac{b_{i-1/2,j}}{\xi_{xi-1/2}} (P_{i,j} - P_{i-1,j}) \right) \\ &\quad + \frac{1}{\xi_{zj}} \frac{1}{\Delta^2} \left(\frac{b_{i,j+1/2}}{\xi_{zj+1/2}} (P_{i,j+1} - P_{i,j}) - \frac{b_{i,j-1/2}}{\xi_{zj-1/2}} (P_{i,j} - P_{i,j-1}) \right) + S_{i,j}. \end{aligned} \quad (7)$$

Note that although only one scalar field P is now considered after elimination, the underlying staggered-grid structure still appears in the parsimonious formulation, eq. (7), through the estimation of the buoyancy parameter at intermediate positions with respect to the pressure gridpoints. Buoyancy at intermediate positions labelled by indices $i \pm 1/2$, $j \pm 1/2$ is computed by arithmetic averaging.

We extract the coefficients that correspond to the staggered-grid five-point stencil (see Fig. 1):

$$\begin{aligned}
 C_1 &= \frac{\omega^2}{K_{i,j}} - \frac{1}{\xi_{xi} \Delta^2} \left(\frac{b_{i+1/2,j}}{\xi_{xi+1/2}} + \frac{b_{i-1/2,j}}{\xi_{xi-1/2}} \right) - \frac{1}{\xi_{zj} \Delta^2} \left(\frac{b_{i,j+1/2}}{\xi_{zj+1/2}} + \frac{b_{i,j-1/2}}{\xi_{zj-1/2}} \right) \\
 C_2 &= \frac{1}{\xi_{xi} \Delta^2} \frac{b_{i-1/2,j}}{\xi_{xi-1/2}} \\
 C_3 &= \frac{1}{\xi_{xi} \Delta^2} \frac{b_{i+1/2,j}}{\xi_{xi+1/2}} \\
 C_4 &= \frac{1}{\xi_{zj} \Delta^2} \frac{b_{i,j-1/2}}{\xi_{zj-1/2}} \\
 C_5 &= \frac{1}{\xi_{zj} \Delta^2} \frac{b_{i,j+1/2}}{\xi_{zj+1/2}}.
 \end{aligned} \tag{8}$$

We have provided the procedure to derive parsimonious staggered-grid FD stencils for the frequency-domain second-order wave equation. In order to analyse the properties of the staggered-grid stencils from a qualitative viewpoint, we now remind the reader of an intrinsic feature of staggered-grid stencils.

Let us assume we want to perform FDTD wave propagation modelling using the time-domain first-order hyperbolic formulation, equation system (1). For the purposes of illustration, the system is discretized for variables P , Q and R on a single non-staggered grid using a centred finite-difference stencil $(-1/2, 0, 1/2)$ for the first-derivative operator. By a non-staggered grid, we define here the single grid built by adding all intermediate points to the classical staggered grids of Fig. 1. If we denote by Δ_{ns} the mesh spacing of the non-staggered grid, then the mesh spacing of the staggered grids would be $\Delta = 2\Delta_{ns}$. The coefficient 0 in the centred FD stencil $(-1/2, 0, 1/2)$ accounts for the non-staggered-grid structure (i.e. by construction, this zero coefficient does not exist when staggered grids are considered). The coefficients $\pm 1/2$ account for the spatial support $2\Delta_{ns}$ of the centred stencil, used to compute the first-order derivative.

We consider a homogeneous medium with a velocity of 4000 m s^{-1} and a density of 2500 kg m^{-3} . A point source is located in the middle of the medium. The source is excited at one single grid node. A time-domain snapshot of the pressure field shows two uncoupled staggered grids: one that is not excited (i.e. the amplitude of the pressure nodes was left to zero) while the other is related to the source position and will provide the simulation we are interested in Fig. 2(a). Snapshots of the two velocity fields (not shown there) also exhibit uncoupled staggered grids, except that the nodes of the two subgrids are not at the same location in the pressure and velocity grids. One may remove the unexcited subgrids in the pressure and velocity grids leading to the first staggered-grid geometry of Fig. 1. The decoupling between the staggered grids shows that the staggered-grid stencil is accurate to second-order in the space increment $2\Delta_{ns}$. This analysis will be applied later to other stencils to compare their accuracy qualitatively.

2.2 Comparison with the classical grid approach

A standard five-point stencil was constructed directly by Pratt & Worthington (1990, eqs B6 and B7). They discretized the second-order hyperbolic acoustic wave equation:

$$\frac{\partial}{\partial x} \left(\frac{1}{\rho(x, z)} \frac{\partial}{\partial x} P(x, z, \omega) \right) + \frac{\partial}{\partial z} \left(\frac{1}{\rho(x, z)} \frac{\partial}{\partial z} P(x, z, \omega) \right) + \frac{\omega^2}{K(x, z)} P(x, z, \omega) = S(x, z, \omega), \tag{9}$$

using the finite-difference approximation of spatial derivatives proposed by Boore (1972, eq. 11) or by Kelly *et al.* (1976). These finite-difference operators are given by:

$$\begin{aligned}
 \left[\frac{\partial}{\partial x} \left(\frac{1}{\rho(x, z)} \frac{\partial}{\partial x} P(x, z, \omega) \right) \right]_{i,j} &\approx \frac{1}{\Delta^2} \left(\frac{1}{\rho_{i+1/2,j}} (P_{i+1,j} - P_{i,j}) - \frac{1}{\rho_{i-1/2,j}} (P_{i,j} - P_{i-1,j}) \right) \\
 \left[\frac{\partial}{\partial z} \left(\frac{1}{\rho(x, z)} \frac{\partial}{\partial z} P(x, z, \omega) \right) \right]_{i,j} &\approx \frac{1}{\Delta^2} \left(\frac{1}{\rho_{i,j+1/2}} (P_{i,j+1} - P_{i,j}) - \frac{1}{\rho_{i,j-1/2}} (P_{i,j} - P_{i,j-1}) \right)
 \end{aligned} \tag{10}$$

where

$$\frac{1}{\rho_{i+1/2,j}} = \frac{1}{2} \left(\frac{1}{\rho_{i+1,j}} + \frac{1}{\rho_{i,j}} \right).$$

An immediate comparison shows that this standard five-point stencil is identical to the previous staggered-grid five-point stencil (eq. 7) away from the PML zones where damping functions $\xi(x)$ and $\xi(z)$ are equal to 1.

This analysis shows the identity of the second-order numerical schemes between the staggered-grid and the standard-grid formulations as long as harmonic averaging of density is considered in the standard-grid formulation.

2.3 The alternative rotated staggered-grid strategy

One may consider that the spatial derivatives of the system of eqns (1) could be discretized along rotated axes of a system (x', z') (Fig. 1). Let us underline that this is not equivalent to a complete rotation because wavefield components are still considered in the

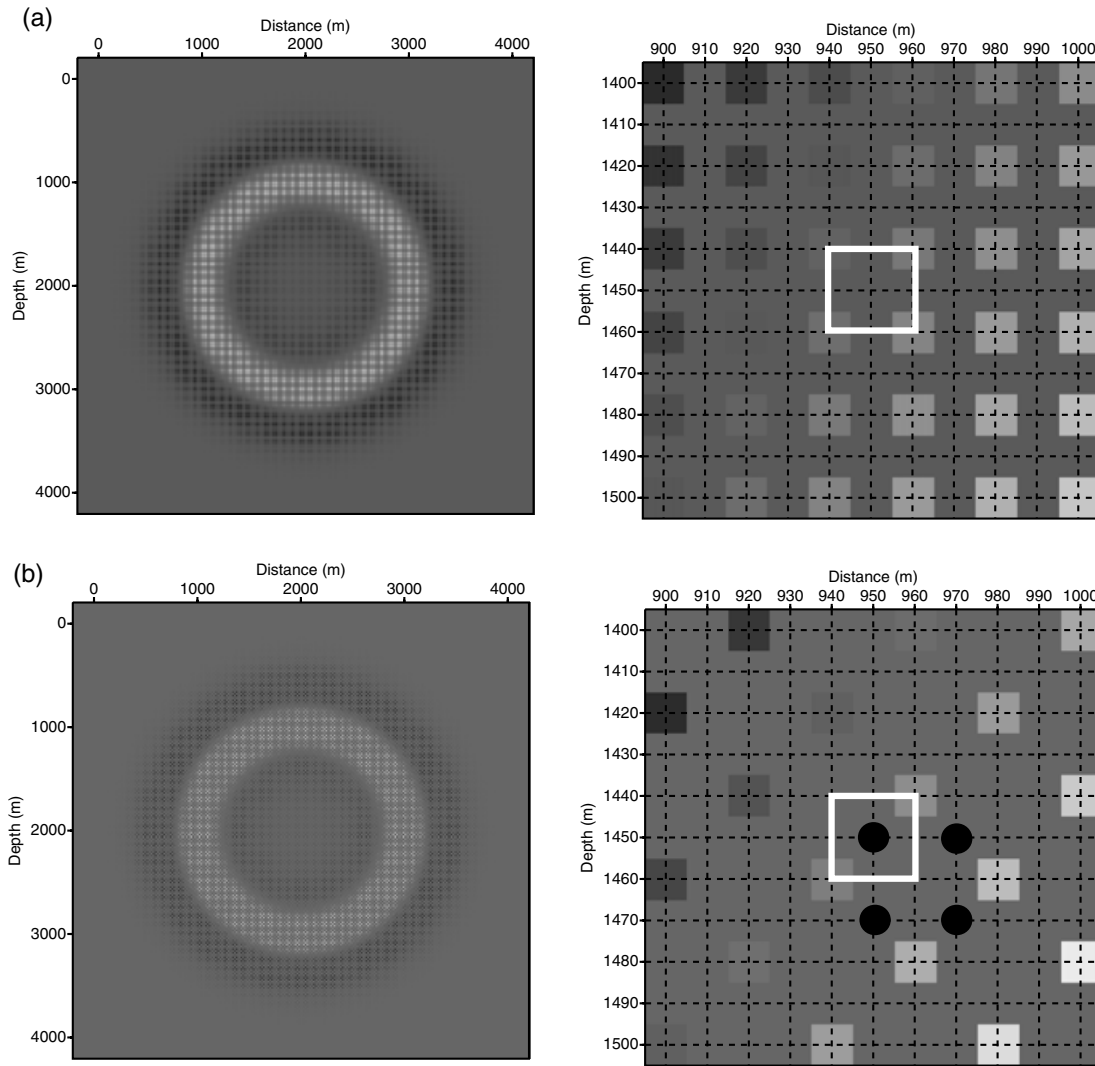


Figure 2. For a non-staggered-grid formulation we show on the left side a snapshot of the pressure field propagating in a homogeneous medium and excited by an impulsive point source. On the right side we show a close-up of this snapshot. The intersections between the dashed lines indicate the locations of the gridpoints. (a) Second-order staggered-grid stencil of coefficients $(-1/2, 0, 1/2)$ for the first derivative is applied: two subgrids are superposed. Only one grid is excited as shown by the zoom. Grey nodes are not excited and could be eliminated. The white square on the zoom delineates the associated staggered-grid cell. (b) Second-order rotated staggered-grid stencil of coefficients $(-1/2\sqrt{2}, 0, 1/2\sqrt{2})$ is applied. Two subgrids are still superposed. The white square still denotes the elementary staggered-grid cell. Note that contrary to the case shown in (a) two gridpoints (the upper left and the bottom right) on the staggered-grid cell have remained unexcited (see text for further explanation). The four black circles delineate one velocity staggered-grid cell. The velocity fields are not accurately computed due to the incomplete excitation of the pressure grid.

old system (x, z) . This complementary approach has been developed in the time domain for the P - SV wave equation by Saenger *et al.* (2000).

Equation system (3) becomes:

$$\begin{aligned}
 \frac{-i\omega\xi_x(x)}{K(x, z)} P_x(x, z, \omega) &= \frac{\sqrt{2}}{2} \left(\frac{\partial Q(x, z, t)}{\partial x'} + \frac{\partial Q(x, z, t)}{\partial z'} \right) + S(x, z, t) \\
 \frac{-i\omega\xi_z(z)}{K(x, z)} P_z(x, z, \omega) &= \frac{\sqrt{2}}{2} \left(-\frac{\partial R(x, z, t)}{\partial x'} + \frac{\partial R(x, z, t)}{\partial z'} \right) \\
 -i\omega Q(x, z, \omega) &= \frac{\sqrt{2}}{2} \frac{b(x, z)}{\xi_x(x)} \left(\frac{\partial P(x, z, t)}{\partial x'} + \frac{\partial P(x, z, t)}{\partial z'} \right) \\
 -i\omega R(x, z, \omega) &= \frac{\sqrt{2}}{2} \frac{b(x, z)}{\xi_z(z)} \left(-\frac{\partial P(x, z, t)}{\partial x'} + \frac{\partial P(x, z, t)}{\partial z'} \right).
 \end{aligned} \tag{11}$$

Equation system (11) is discretized using second-order centred staggered-grid stencils:

$$\begin{aligned} \left[\frac{\partial Q}{\partial x'} \right]_{i,j} &\approx \frac{1}{\sqrt{2}} \frac{1}{\Delta} (Q_{i+1/2,j-1/2} - Q_{i-1/2,j+1/2}) \\ \left[\frac{\partial Q}{\partial z'} \right]_{i,j} &\approx \frac{1}{\sqrt{2}} \frac{1}{\Delta} (Q_{i+1/2,j+1/2} - Q_{i-1/2,j-1/2}). \end{aligned} \quad (12)$$

The configuration of this second staggered grid is shown in Fig. 1. The two particle velocity components are defined at the same node. These nodes are different from the nodes of the first staggered grid. In contrast, the pressure is defined at the same nodes as for the first staggered grid. Using the same procedure as for the classical Cartesian coordinate system, we obtain the following discretized wave equation:

$$\begin{aligned} &\left\{ \frac{-\omega^2}{K_{i,j}} + \frac{1}{4\Delta^2} \left[b_{i+1/2,j-1/2} \left(\frac{1}{\xi_{xi}\xi_{xi+1/2}} + \frac{1}{\xi_{zi}\xi_{zj-1/2}} \right) + b_{i-1/2,j+1/2} \left(\frac{1}{\xi_{xi}\xi_{xi-1/2}} + \frac{1}{\xi_{zi}\xi_{zj+1/2}} \right) \right. \right. \\ &\quad \left. \left. + b_{i+1/2,j+1/2} \left(\frac{1}{\xi_{xi}\xi_{xi+1/2}} + \frac{1}{\xi_{zi}\xi_{zj+1/2}} \right) + b_{i-1/2,j-1/2} \left(\frac{1}{\xi_{xi}\xi_{xi-1/2}} + \frac{1}{\xi_{zi}\xi_{zj-1/2}} \right) \right] \right\} P_{i,j} \\ &+ \frac{1}{4\Delta^2} \left\{ -P_{i+1,j} \left[b_{i+1/2,j-1/2} \left(\frac{1}{\xi_{xi}\xi_{xi+1/2}} - \frac{1}{\xi_{zi}\xi_{zj-1/2}} \right) + b_{i+1/2,j+1/2} \left(\frac{1}{\xi_{xi}\xi_{xi+1/2}} - \frac{1}{\xi_{zi}\xi_{zj+1/2}} \right) \right] \right. \\ &\quad - P_{i-1,j} \left[b_{i-1/2,j+1/2} \left(\frac{1}{\xi_{xi}\xi_{xi-1/2}} - \frac{1}{\xi_{zi}\xi_{zj+1/2}} \right) + b_{i-1/2,j-1/2} \left(\frac{1}{\xi_{xi}\xi_{xi-1/2}} - \frac{1}{\xi_{zi}\xi_{zj-1/2}} \right) \right] \\ &\quad + P_{i,j+1} \left[b_{i-1/2,j+1/2} \left(\frac{1}{\xi_{xi}\xi_{xi-1/2}} - \frac{1}{\xi_{zi}\xi_{zj+1/2}} \right) + b_{i+1/2,j+1/2} \left(\frac{1}{\xi_{xi}\xi_{xi+1/2}} - \frac{1}{\xi_{zi}\xi_{zj+1/2}} \right) \right] \\ &\quad + P_{i,j-1} \left[b_{i+1/2,j-1/2} \left(\frac{1}{\xi_{xi}\xi_{xi+1/2}} - \frac{1}{\xi_{zi}\xi_{zj-1/2}} \right) + b_{i-1/2,j-1/2} \left(\frac{1}{\xi_{xi}\xi_{xi-1/2}} - \frac{1}{\xi_{zi}\xi_{zj-1/2}} \right) \right] \\ &\quad - P_{i+1,j-1} b_{i+1/2,j-1/2} \left(\frac{1}{\xi_{xi}\xi_{xi+1/2}} + \frac{1}{\xi_{zi}\xi_{zj+1/2}} \right) \\ &\quad - P_{i-1,j+1} b_{i-1/2,j+1/2} \left(\frac{1}{\xi_{xi}\xi_{xi-1/2}} + \frac{1}{\xi_{zi}\xi_{zj+1/2}} \right) \\ &\quad - P_{i+1,j+1} b_{i+1/2,j+1/2} \left(\frac{1}{\xi_{xi}\xi_{xi+1/2}} + \frac{1}{\xi_{zi}\xi_{zj+1/2}} \right) \\ &\quad \left. \left. - P_{i-1,j-1} b_{i-1/2,j-1/2} \left(\frac{1}{\xi_{xi}\xi_{xi-1/2}} + \frac{1}{\xi_{zi}\xi_{zj-1/2}} \right) \right\} = S_{i,j}. \end{aligned} \quad (13)$$

This system of equations defines a nine-point stencil inside the whole domain. If we now consider gridpoints outside the PML layers (i.e. $\xi_x = \xi_z = 1$) and regroup terms with respect to buoyancy, the equation system (13) reduces to

$$\begin{aligned} \frac{-\omega^2}{K_{i,j}} P_{i,j} &= \frac{1}{2\Delta^2} [b_{i+1/2,j-1/2}(P_{i+1,j-1} - P_{i,j}) + b_{i-1/2,j+1/2}(P_{i-1,j+1} - P_{i,j}) \\ &\quad + b_{i+1/2,j+1/2}(P_{i+1,j+1} - P_{i,j}) + b_{i-1/2,j-1/2}(P_{i-1,j-1} - P_{i,j})] + S_{i,j}. \end{aligned} \quad (14)$$

Outside PML zones, eq. (14) defines a five-point rotated stencil of coefficients:

$$\begin{aligned} C_1 &= \frac{\omega^2}{K_{i,j}} + \frac{1}{2\Delta^2} (b_{i+1/2,j-1/2} + b_{i-1/2,j+1/2} + b_{i+1/2,j+1/2} + b_{i-1/2,j-1/2}) \\ R_2 &= \frac{1}{2\Delta^2} b_{i-1/2,j} \\ R_3 &= \frac{1}{2\Delta^2} b_{i+1/2,j} \\ R_4 &= \frac{1}{2\Delta^2} b_{i,j-1/2} \\ R_5 &= \frac{1}{2\Delta^2} b_{i,j+1/2}, \end{aligned} \quad (15)$$

with a geometrical distribution given in Fig. 1. This rotated staggered-grid five-point stencil differs from the previous one based on the classical unrotated staggered-grid strategy. If one considers a homogeneous density, the stencil of the system of eq. (15) is identical to the stencil of Jo *et al.* (1996) when using $a = 0$; i.e. considering only the discretization of the Laplacian term on the rotated coordinate system (see eq. 3 in Jo *et al.* 1996). The approach of Jo *et al.* (1996) was extended to the case of heterogeneous density models by Štekl (1997). The stencil developed by Štekl (1997) when using $a = 0$ is identical to the one of the system of eq. (15).

As for the first staggered-grid geometry (see the end of the section 2.1) we perform wave propagation over a single non-staggered grid with a mesh spacing Δ_{ns} , where variables P , Q and R are defined at each node using a centred finite-different stencil $(-1/2\sqrt{2}, 0, 1/2\sqrt{2})$ for the first-derivative operator approximated on the rotated grid. The coefficients $\pm 1/2\sqrt{2}$ account for the spatial support $2\sqrt{2}\Delta_{ns}$ of the centred stencil, used to compute the first-order derivative along the bisectrices. Again, the impulsional source is excited at one grid node. The

pressure snapshot shows that, again, one subgrid stays strictly unexcited when considering a point source (Fig. 2b). Nevertheless, we observed a difference compared with the first staggered-grid case. One can note in Fig. 2(b) that only one point out of five was excited on the full grid (i.e. a non-staggered grid) while the rotated staggered-grid structure shown in Fig. 1 would suggest that one gridpoint out of two should have been excited. The white square in Fig. 2b delineates the elementary staggered-grid pressure cell associated with the rotated staggered-grid stencil (Fig. 1). One can note that two of the four nodes at the corners of the cell (the upper left and the bottom right) have remained unexcited (Fig. 2b), contrary to the case of the classical staggered-grid stencil for which the four nodes have been excited (Fig. 2a). The fact that half of the pressure staggered-grid nodes remained unexcited implies that the spatial derivatives of the pressure fields, and hence the velocity fields, are not correctly computed. Indeed, both the horizontal and vertical differential operator stencils associated with the rotated staggered-grid strategy involve the four points surrounding the central node where the derivative has to be estimated (see eqs 8, 9, 10 and 11 in Saenger *et al.* 2000). Two of these four nodes remained unexcited during the simulation leading to an erroneous estimation of the spatial partial derivatives of the pressure field. As an illustration, the black circles in Fig. 2(b) delineate a staggered cell for velocity fields. The upper left velocity node is computed from the surrounding four pressure nodes indicated by the white square—two of them are zero.

This behaviour of the rotated staggered-grid stencil (namely, the incomplete excitation of the pressure staggered grid when an impulsional point source is considered) suggests that its dispersion properties are less good than that of the classical staggered-grid stencil. Note, however, that a simple way to remove this artefact is to strengthen the grid coupling by smoothing the source spatial distribution, namely by spreading the point source excitation on several adjacent nodes (see also the section entitled ‘Source excitation in the wavelet domain’ in Operto *et al.* 2002). Moreover, the space increment of $2\sqrt{2}\Delta_{\text{ns}}$ along the rotated direction of spatial differentiations is greater than that of the classical staggered-grid stencil for which a space increment of $2\Delta_{\text{ns}}$ is considered along the unrotated direction of spatial differentiations. A comparable accuracy of the classical and the rotated staggered-grid stencils is reached when the space increment along the direction of spatial differentiations is the same (see Fig. 4 in Saenger *et al.* 2000, in the case of the elastic wave equation). This requires to use a grid interval of $\Delta/\sqrt{2}$ when using the rotated staggered-grid stencil instead of Δ for the classical staggered grid.

3 IMPROVED FINITE-DIFFERENCE DISCRETIZATION

How may we increase the accuracy of our numerical operators while maintaining computational efficiency? One strategy is to augment the accuracy by incorporating gridpoints in the FD stencil around the collocation along several directions (Jo *et al.* 1996; Štekl & Pratt 1998; Shin & Sohn 1998). This leads to the so-called mixed-grid stencils. Another approach consists of increasing the accuracy of FD operators along Cartesian axes associated with the derivative directions (either the classical or rotated Cartesian axes) by increasing the order of the operator.

3.1 The mixed-grid stencil

When considering the standard five-point stencil, numerical dispersion is most significant along bisectrices. This dispersion is reduced by adding four additional points to the five-point stencil. Jo *et al.* (1996) and Štekl (1997) have combined the acoustic wave equations written in the original Cartesian coordinate system (eq. 10) and the 45° -rotated coordinate system (eq. 11). The two coordinate systems are discretized, such that they define the same numerical grid for the pressure field. This implies that the mesh spacing in the rotated coordinate system is equal to $\sqrt{2}\Delta$. Combination of the wave equations in the two coordinate systems leads to a mixed-grid stencil that incorporates nine points (Fig. 3). In the acoustic case, this combination requires only the development of the derivative approximations on the Cartesian and the 45° -rotated grids, since the pressure is a scalar field. In the elastic case, additional algebra is required to manipulate vector fields (see Štekl & Pratt 1998, for details). The mixed-operator approach is a state-of-the-art tool in FDFD seismic wave modelling for efficient and accurate modelling (Jo *et al.* 1996; Štekl & Pratt 1998; Shin & Sohn 1998).

Discretization of the spatial derivatives on the 45° -rotated grid gives the following stencil formulation:

$$\begin{aligned} \left[\frac{\partial}{\partial x'} \left(\frac{1}{\rho(x', z')} \frac{\partial}{\partial x'} P(x', z', \omega) \right) \right]_{i,j} &\approx \frac{1}{2\Delta^2} \left(\frac{1}{\rho_{i+1/2, j-1/2}} (P_{i+1, j-1} - P_{i, j}) - \frac{1}{\rho_{i-1/2, j+1/2}} (P_{i, j} - P_{i-1, j+1}) \right) \\ \left[\frac{\partial}{\partial z'} \left(\frac{1}{\rho(x', z')} \frac{\partial}{\partial z'} P(x', z', \omega) \right) \right]_{i,j} &\approx \frac{1}{2\Delta^2} \left(\frac{1}{\rho_{i+1/2, j+1/2}} (P_{i+1, j+1} - P_{i, j}) - \frac{1}{\rho_{i-1/2, j-1/2}} (P_{i, j} - P_{i-1, j-1}) \right), \end{aligned} \quad (16)$$

which is identical to the parsimonious rotated staggered-grid formulation described previously. We denote differential operators in the following compact form:

$$\begin{aligned} \Gamma_{i,j} &= \left[\frac{\partial}{\partial x} \left(\frac{1}{\rho(x, z)} \frac{\partial}{\partial x} P(x, z, \omega) \right) \right]_{i,j} + \left[\frac{\partial}{\partial z} \left(\frac{1}{\rho(x, z)} \frac{\partial}{\partial z} P(x, z, \omega) \right) \right]_{i,j} \\ \Theta_{i,j} &= \left[\frac{\partial}{\partial x'} \left(\frac{1}{\rho(x', z')} \frac{\partial}{\partial x'} P(x', z', \omega) \right) \right]_{i,j} + \left[\frac{\partial}{\partial z'} \left(\frac{1}{\rho(x', z')} \frac{\partial}{\partial z'} P(x', z', \omega) \right) \right]_{i,j}. \end{aligned} \quad (17)$$

We combine operators to an improved discrete wave equation that defines the mixed-grid stencil:

$$a\Gamma_{i,j} + (1-a)\Theta_{i,j} + \left[\frac{\omega^2}{K(x, z)} P(x, z, \omega) \right]_{i,j} = S_{i,j}. \quad (18)$$

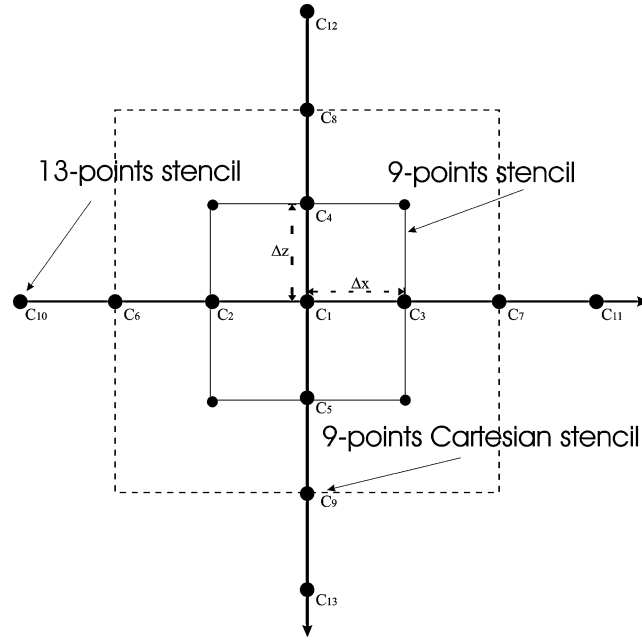


Figure 3. Illustration of three different stencils used for the finite-difference discretization of the acoustic wave equation. The nine-point mixed-grid stencil and the 13-point staggered-grid stencil are considered for approximations of fourth-order accuracy. Another nine-point stencil, called the nine-point Cartesian stencil, can be developed for a homogeneous medium when considering quantities along Cartesian axes.

The averaging coefficient a accounts for the coupling between grid nodes that lie on the Cartesian grid (black dots) and the rotated grid (grey dots) (Fig. 1).

This analysis demonstrates the connection between staggered-grid and mixed-grid formulations. The mixed operator approach linearly combines two staggered-grid formulations based on a second-order centred approximation of the first derivative in the hyperbolic system of eqs (1) and (11). As we have shown, the two staggered-grid stencils lead to different five-point stencils. Combination of the two stencils gives a nine-point stencil that has a very compact geometry (Fig. 3). The two staggered-grid systems do not have the same geometry because the particle velocities do not follow the same configuration on the two staggered-grid formulations (Fig. 1). This also implies that the mixed-grid stencil cannot be implemented in the first-order hyperbolic formulation using staggered grids (i.e. without adding additional intermediate grid nodes). Only the parsimonious formulation can be implemented since it eliminates those wavefields for which the gridpoints are not located on the same numerical grids, i.e. the particle velocity wavefields.

Does this discrete construction of derivative stencils avoid the decoupling of subgrid structures? Again, we performed wave propagation simulations using the mixed-grid stencil for a point source in the same homogeneous medium we have considered for the staggered-grid stencil simulations. The mixed-grid formulation (eq. 18) is recast into the framework of the first-order hyperbolic formulation, which gives:

$$\frac{\partial P(x, z, t)}{\partial t} = K(x, z) \left[a \left(\frac{\partial Q(x, z, t)}{\partial x} + \frac{\partial R(x, z, t)}{\partial z} \right) + (1 - a) \left(\frac{\partial Q'(x', z', t)}{\partial x'} + \frac{\partial R'(x', z', t)}{\partial z'} \right) \right] + S(x, z, t) \quad (19)$$

$$\begin{aligned} \frac{\partial Q(x, z, t)}{\partial t} &= b(x, z) \frac{\partial P(x, z, t)}{\partial x} \\ \frac{\partial R(x, z, t)}{\partial t} &= b(x, z) \frac{\partial P(x, z, t)}{\partial z} \\ \frac{\partial Q'(x', z', t)}{\partial t} &= b(x', z') \frac{\partial P(x', z', t)}{\partial x'} \\ \frac{\partial R'(x', z', t)}{\partial t} &= b(x', z') \frac{\partial P(x', z', t)}{\partial z'}, \end{aligned} \quad (20)$$

where Q' and R' are the acoustic components of the particle velocity vector in the rotated coordinate system. Again, the first-derivative operator is approximated by a centred FD stencil $(-1/2, 0, 1/2)$ on the full grid.

The snapshot of the pressure field shows decoupled grid effects, i.e. an unexcited grid is still present (Fig. 4a). Therefore, combining the Cartesian five-point stencil and the rotated five-point stencil does not couple all nodes of the full pressure grid. The pressure gridpoints that are excited by the combined stencil are only coupled at their common staggered-grid locations (Fig. 1). The pressure-grid coupling is foreseeable since the locations of the excited gridpoints of the rotated staggered-grid stencil (Fig. 2b) and the classical staggered-grid stencil (Fig. 2a) coincide. Note, however, that twice as many gridpoints are excited by the classical staggered-grid stencil as the rotated one (compare Figs 2a and 2b).

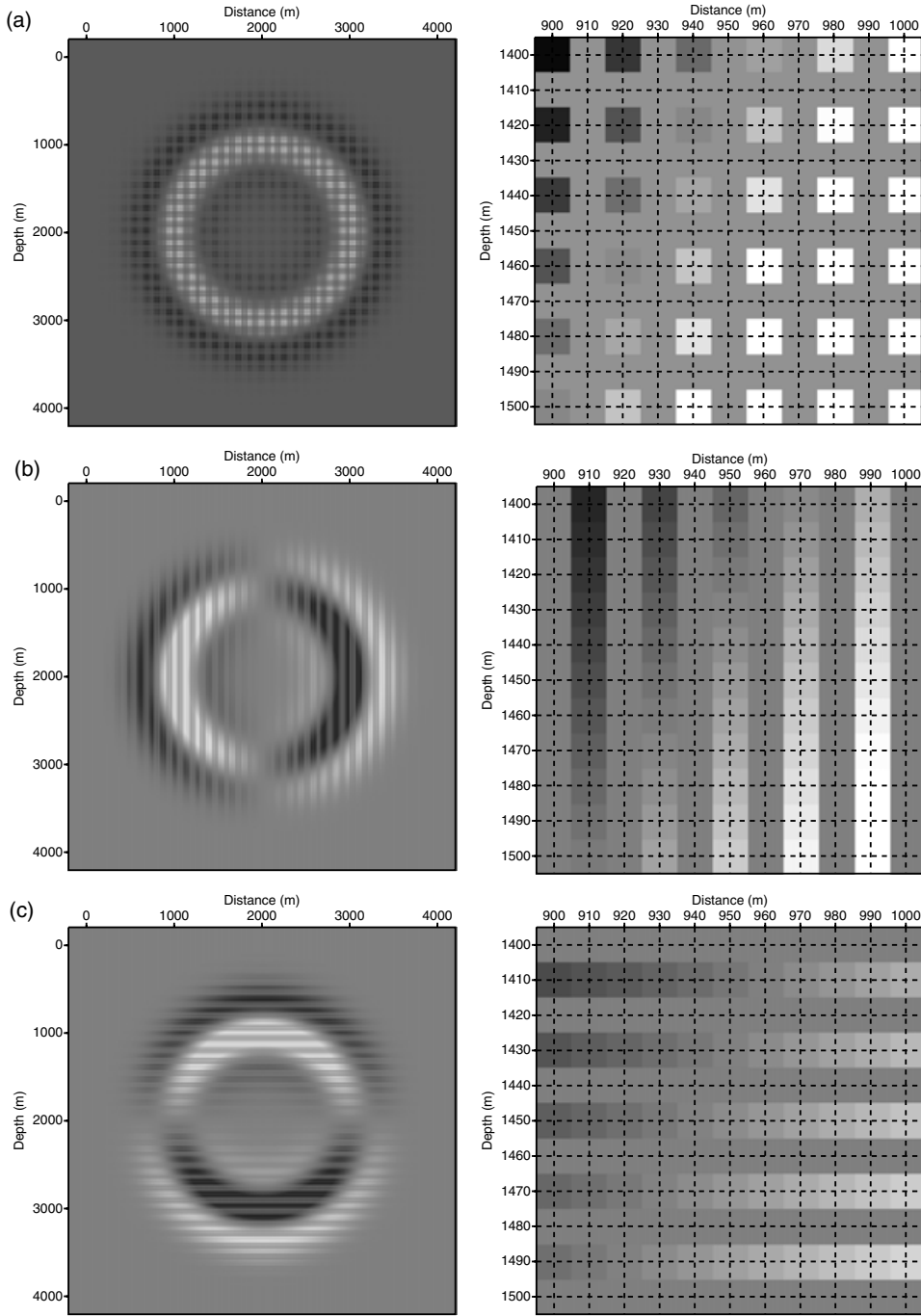


Figure 4. (a, left) Snapshot of the pressure field propagating in a homogeneous medium and excited by an impulsive point source. The mixed-grid stencil is implemented in the first-order hyperbolic formulation of the acoustic wave equation without acceleration averaging: two uncoupled grids are observed. The excited grid is the combination of the excited grids of Figs 2(a) and (b). (a, right) Close-up of the snapshot. The intersection between the dashed lines indicates the location of the gridpoints. (b, left) Snapshot of the additional variable Q that is analogous to the horizontal velocity snapshot for the elastic wave propagation. (b, right) Close-up. (c, left) Snapshot of the additional variable R : vertical velocity snapshot. (c, right) Close-up. The mixed-grid formulation partially couples the two combined staggered-grid stencils. In fact, the combined pressure grid shown in (a) excites two different staggered velocity grids. Therefore, additional coupling of differently excited grids by an acceleration averaging strategy is a key element of this stencil, not just a numerical improvement.

We plot the snapshots for the particle velocities in the Cartesian coordinate system, $0.5[Q + \frac{\sqrt{2}}{2}(Q' + R')]$ and $0.5[R + \frac{\sqrt{2}}{2}(-Q' + R')]$, in Fig. 4. We observe that the excited velocity grids for the two components have nodes at different locations. The coupling of the two grids is ensured by the excitation of the pressure grid, as is shown in Fig. 4(a). The coupling of the two velocity grids partially fills up the unexcited grids (Figs 4b and c) vertically and horizontally for the horizontal and vertical velocities respectively. The observed pattern implies that the coupling of the two stencils is not optimal. Moreover, we deduce second-order accuracy in the space increment Δ for the mixed-grid stencil.

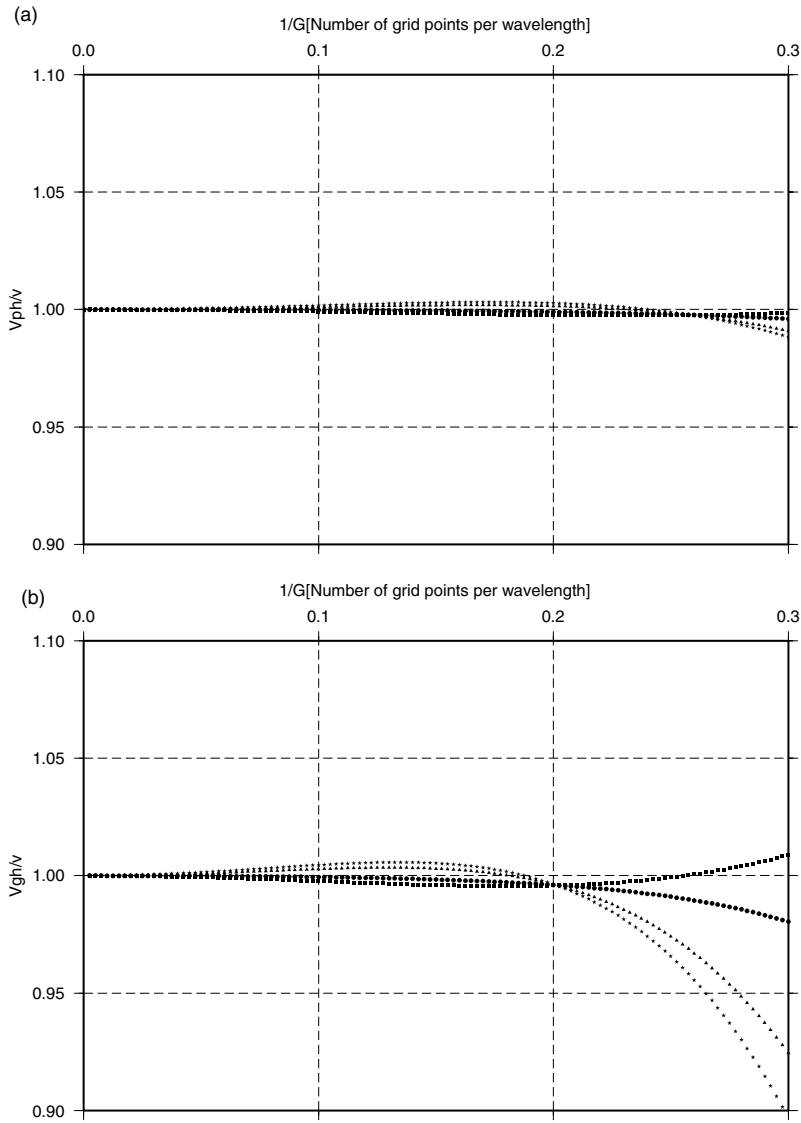


Figure 5. Relative phase v_{ph} and group v_{gr} velocity curves for the mixed-grid formulation. We use similar optimization coefficients to Jo *et al.* (1996): $a = 0.5461$, $c = 0.6248$, $d = 0.9381 \times 10^{-1}$ and $e = 0.25[(1 - 4)(d - c)]$. Propagation angles range from 0° to 45° by in steps of 15° from the vertical. The curves are denoted by stars, triangles, circles and squares respectively.

It was already noted that the dispersion of the mixed-grid stencil is more significant than that of the second-order staggered-grid stencil, in the classical coordinate system (compare Figs 2 and 5 in Jo *et al.* 1996). This is in agreement with the partial coupling of the velocity grids in the mixed-grid stencil. The unfavourable coupling of grids degrades the accuracy of the stencil. Therefore, another feature is introduced in the mixed-grid stencil in order to strengthen the subgrid couplings leading to an improvement in modelling accuracy.

In view of this, the pressure acceleration term $\omega^2/K(x, z)$ should not be taken as a term implying only the collocation point (the so-called lump approximation): one may approximate it using a weighted average over the mixed operator stencil nodes, as is done in finite-element modelling (Zienkiewicz & Morgan 1982). This averaging procedure couples the subgrids. In spirit, the procedure which consists of averaging the mass acceleration term is close to the smoothing of the spatial distribution of the source suggested for FDTD modelling at the end of section 2.3.

The operator is defined as:

$$\left[\frac{\omega^2}{K(x, z)} P \right]_{i,j} \Rightarrow \frac{\omega^2}{K(x, z)} \left(cP_{i,j} + d(P_{i+1,j} + P_{i-1,j} + P_{i,j+1} + P_{i,j-1}) + \frac{1-c-4d}{4}(P_{i+1,j+1} + P_{i-1,j+1} + P_{i+1,j-1} + P_{i-1,j-1}) \right), \quad (21)$$

where c and d are two additional averaging coefficients accounting for the coupling between the Cartesian and the 45° -rotated grid. Numerically accurate results, up to four points per shortest wavelength, are guaranteed by an optimization technique that determines the averaging coefficients

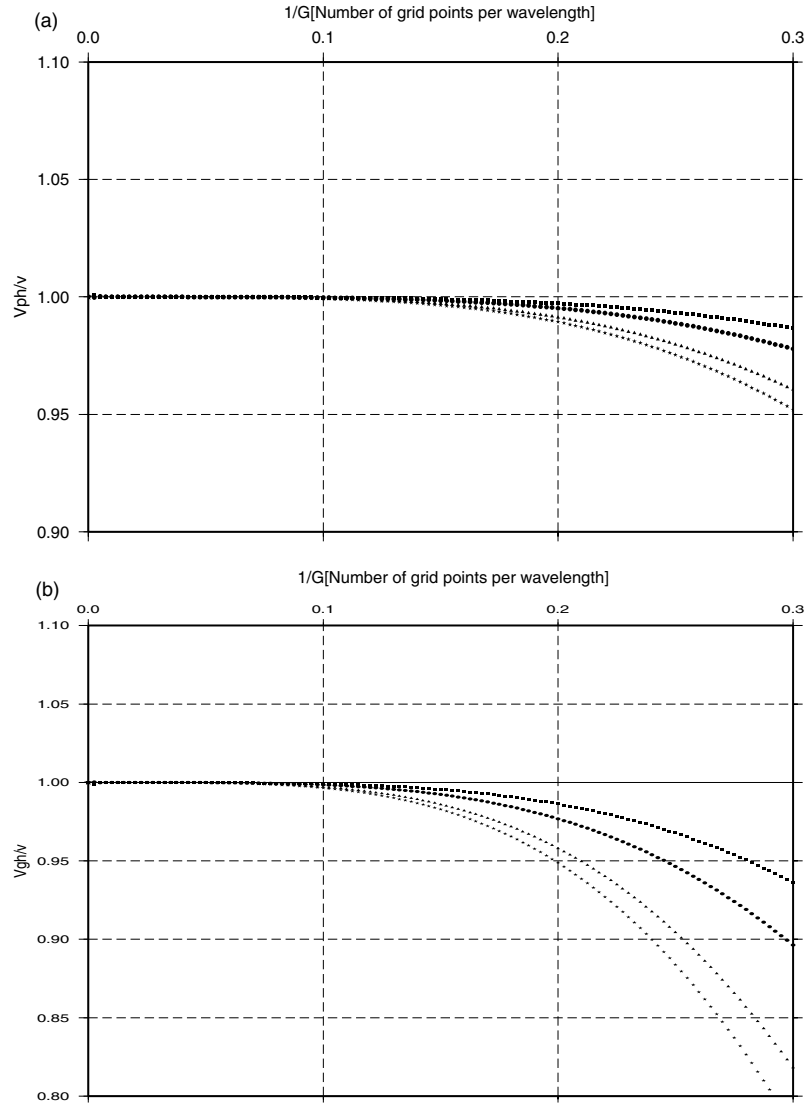


Figure 6. Relative phase v_{ph} and group v_{gr} velocity curves for the staggered-grid formulation using fourth-order staggered-grid stencils ($\alpha_1 = 9/8$ and $\alpha_2 = -1/24$). We use the same symbols for propagation angles as in Fig. 5.

such that the phase velocity dispersion is minimized. Similar optimizations have been done for the FDTD approach by Holberg (1987). The optimal coefficients computed by Jo *et al.* (1996) are $a = 0.5461$, $c = 0.6248$ and $d = 0.09381$. The value for the coefficient $1 - c - 4d = 0.1297 \times 10^{-5}$ is negligible (Štekl 1997) and leads to a five-point distribution of the pressure acceleration instead of nine points. Therefore, the complete stencil involving nine points is described by the following factors (Fig. 3):

$$\begin{aligned}
 C_1 &= c \frac{\omega^2}{K_{i,j}} - \frac{a}{\Delta^2} \left(\frac{1}{\rho_{i+1/2,j}} + \frac{1}{\rho_{i-1/2,j}} + \frac{1}{\rho_{i,j-1/2}} + \frac{1}{\rho_{i,j+1/2}} \right) \\
 &\quad - \frac{1-a}{2\Delta^2} \left(\frac{1}{\rho_{i+1/2,j-1/2}} + \frac{1}{\rho_{i-1/2,j+1/2}} + \frac{1}{\rho_{i+1/2,j+1/2}} + \frac{1}{\rho_{i-1/2,j-1/2}} \right) \\
 C_2 &= c \frac{\omega^2}{K_{i,j}} + \frac{a}{\Delta^2} \frac{1}{\rho_{i-1/2,j}} \\
 C_3 &= c \frac{\omega^2}{K_{i,j}} + \frac{a}{\Delta^2} \frac{1}{\rho_{i+1/2,j}} \\
 C_4 &= c \frac{\omega^2}{K_{i,j}} + \frac{a}{\Delta^2} \frac{1}{\rho_{i,j-1/2}} \\
 C_5 &= c \frac{\omega^2}{K_{i,j}} + \frac{a}{\Delta^2} \frac{1}{\rho_{i,j+1/2}}
 \end{aligned}$$

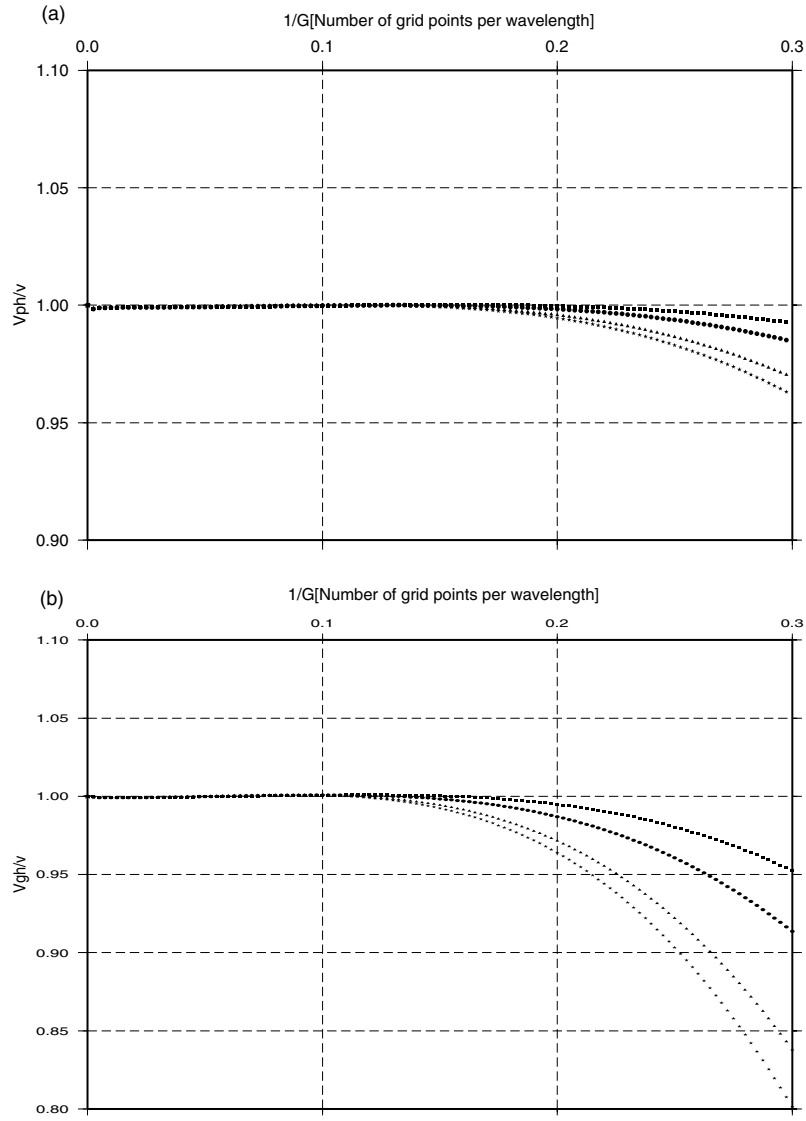


Figure 7. Relative phase v_{ph} and group v_{gr} velocity curves for the optimized staggered-grid stencil. The operator coefficients used for the numerical differentiation are $\alpha_1 = 1.13824281853071$ and $\alpha_2 = -4.64142728435701 \times 10^{-02}$. We use the same symbols for propagation angles as in Fig. 5.

$$\begin{aligned}
 R_1 &= \frac{1-a}{\Delta^2} \frac{1}{\rho_{i-1/2,j-1/2}} \\
 R_2 &= \frac{1-a}{\Delta^2} \frac{1}{\rho_{i+1/2,j-1/2}} \\
 R_3 &= \frac{1-a}{\Delta^2} \frac{1}{\rho_{i-1/2,j+1/2}} \\
 R_4 &= \frac{1-a}{\Delta^2} \frac{1}{\rho_{i+1/2,j+1/2}}.
 \end{aligned} \tag{22}$$

Although partial derivatives are approximated by second-order finite-difference operators, we expect this scheme to behave as a fourth-order operator with respect to accuracy, since both mixed-grid and fourth-order staggered-grid stencils require comparable discretization rules (i.e. five gridpoints per wavelength) (Levander 1988; Jo *et al.* 1996). Moreover, the numerical efficiency should be optimal because it is a compact stencil. Numerical anisotropy is reduced as suggested by the stencil geometry (Fig. 3). Nevertheless, a more quantitative comparison should be given by a dispersion analysis. We discuss this after we have accomplished the stencil construction.

One must keep in mind that the acceleration averaging technique improves the modelling accuracy for a homogeneous medium. Since averaging is a smoothing technique it may pollute the solution in the presence of sharp boundaries. Let us also underline that the comparison through the first-order hyperbolic formulation leads to an original implementation of a PML absorbing boundary condition for the two

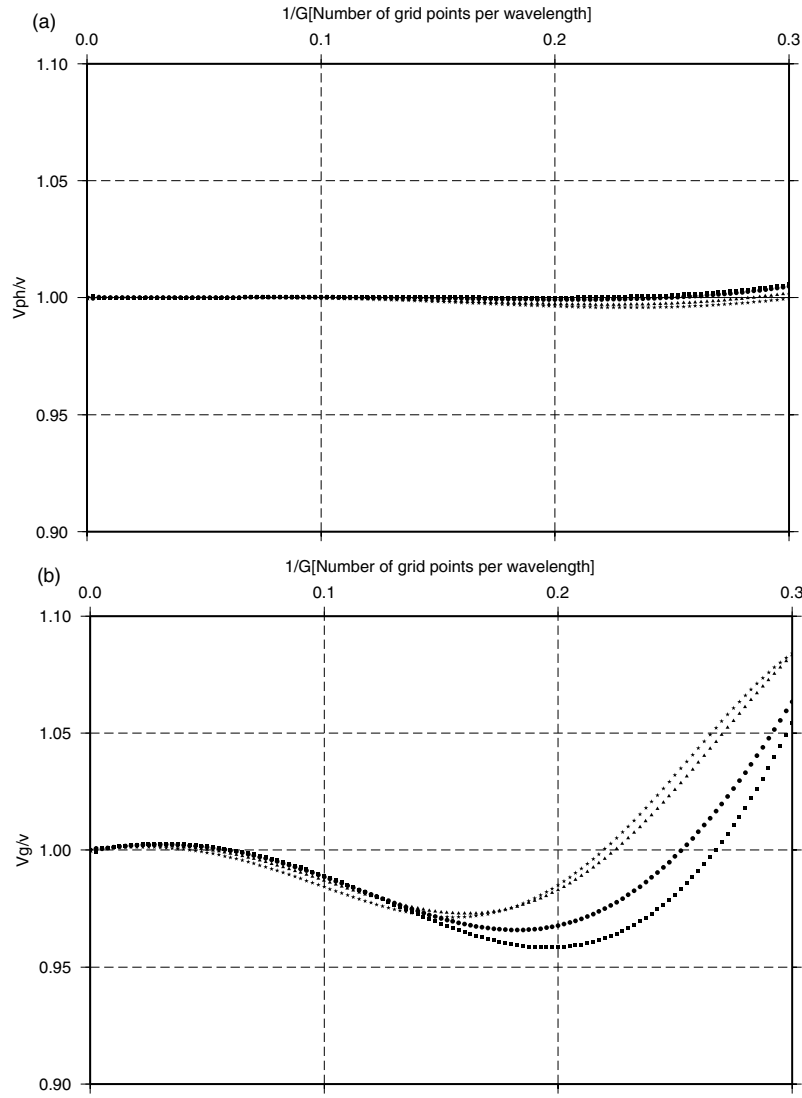


Figure 8. Relative phase v_{ph} and group v_{gr} velocity curves for the staggered-grid formulation using fourth-order staggered-grid stencils combined with the acceleration averaging. We use the same symbols for propagation angles as in Fig. 5. The acceleration averaging significantly improves the phase velocity dispersion curve (compare with Fig. 6).

staggered-grid stencils in the Cartesian and rotated coordinate system (eqs 7 and 13) and therefore for the mixed-grid stencil. An original nine-point PML stencil has been constructed for the mixed-grid stencil, whilst only an approximate five-point stencil has been used previously inside PML zones, as discussed by Dessa (2001) and Hustedt (2002).

In the numerical examples presented later on, we have combined the PML absorbing boundary condition with the 45° one-way paraxial condition (condition A3 of eq. 10 in Clayton & Engquist 1977) at the outer edges of the model.

3.2 Fourth-order finite-difference discretization

Now we investigate a second type of approach to improve the accuracy of the acoustic wave modelling. We use fourth-order FD operators in only a single Cartesian coordinate system.

3.2.1 The homogeneous Cartesian nine-point stencil

The first possible approach considers a fourth-order finite-difference approximation of the second derivative. A centred FD stencil along one axis of coefficients $(-1/12, 16/12, -30/12, 16/12, -1/12)$ can be deduced by classical Taylor expansion analysis (Nougier 1989). This leads to a nine-point stencil for the Laplacian. The geometry of this stencil is shown in Fig. 3 (see the nine-point Cartesian stencil). This approach is limited to homogeneous density models and is mentioned for purpose of completeness only. Therefore, it will not be investigated further.

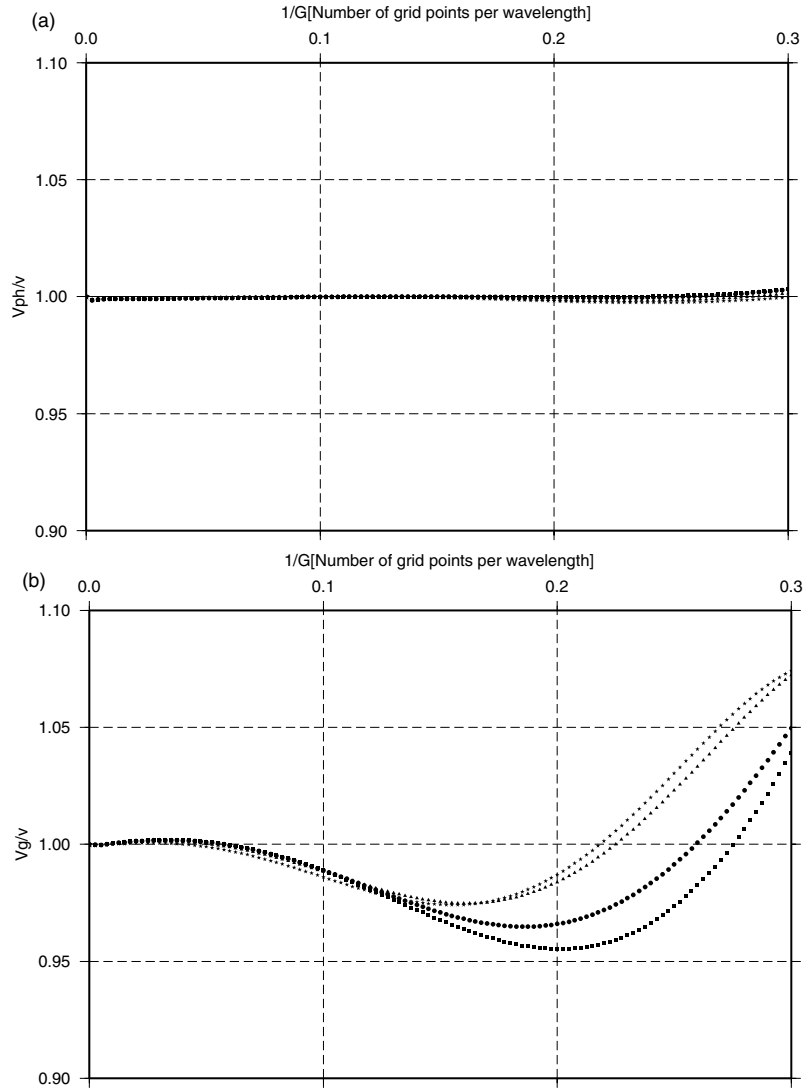


Figure 9. Relative phase v_{ph} and group v_{gr} velocity curves for the optimized staggered-grid stencil combined with acceleration averaging. We use the same symbols for propagation angles as in Fig. 5. The mass averaging significantly improves the phase velocity dispersion curve (compare with Fig. 7).

3.2.2 The fourth-order staggered-grid stencil

In order to account for heterogeneous density models, we come back to the first-order hyperbolic formulation and use fourth-order spatial derivative approximations for the first derivative on staggered grids (Levander 1988).

$$\begin{aligned} \left[\frac{\partial Q}{\partial x} \right]_{i,j} &\approx \frac{1}{\Delta} \left(\frac{9}{8} (Q_{i+1/2,j} - Q_{i-1/2,j}) - \frac{1}{24} (Q_{i+3/2,j} - Q_{i-3/2,j}) \right) \\ \left[\frac{\partial R}{\partial z} \right]_{i,j} &\approx \frac{1}{\Delta} \left(\frac{9}{8} (R_{i,j+1/2} - R_{i,j-1/2}) - \frac{1}{24} (R_{i,j+3/2} - R_{i,j-3/2}) \right). \end{aligned} \quad (23)$$

The fourth-order staggered-grid stencil is the most commonly used in the time domain, since it is supposed to provide the best trade-off between numerical accuracy and computational efficiency.

In the following, we develop the fourth-order staggered-grid stencil in the classical Cartesian coordinate system. A similar derivation could be developed in the rotated frame by simply considering fourth-order finite-difference formulae along the 45° -rotated axes. These higher-order schemes are deduced from the work of Saenger *et al.* (2000) and have been used by Cruz-Atienza & Virieux (2003) for time-domain crack modelling.

The resulting stencil for the second-order wave equation incorporates 13 grid points (details are given in Appendix A). The staggered-grid stencil is plotted in Fig. 3. We apply a similar derivation procedure as the one for the case of the second-order derivation approximation, and

obtain for the pressure wavefield P :

$$\begin{aligned}
 \frac{-\omega^2}{K_{i,j}} P_{i,j} = & \frac{1}{\Delta^2 \xi_i} \left\{ \frac{9}{8} \left[\frac{b_{i+1/2,j}}{\xi_{xi+1/2}} \left(\frac{9}{8} (P_{i+1,j} - P_{i,j}) - \frac{1}{24} (P_{i+2,j} - P_{i-1,j}) \right) \right. \right. \\
 & - \left. \frac{b_{i-1/2,j}}{\xi_{xi-1/2}} \left(\frac{9}{8} (P_{i,j} - P_{i-1,j}) - \frac{1}{24} (P_{i+1,j} - P_{i-2,j}) \right) \right] \\
 & - \frac{1}{24} \left[\frac{b_{i+3/2,j}}{\xi_{xi+3/2}} \left(\frac{9}{8} (P_{i+2,j} - P_{i+1,j}) - \frac{1}{24} (P_{i+3,j} - P_{i,j}) \right) \right. \\
 & - \left. \left. \frac{b_{i-3/2,j}}{\xi_{xi-3/2}} \left(\frac{9}{8} (P_{i-1,j} - P_{i-2,j}) - \frac{1}{24} (P_{i,j} - P_{i-3,j}) \right) \right] \right\} \\
 & + \frac{1}{\Delta^2 \xi_j} \left\{ \frac{9}{8} \left[\frac{b_{i,j+1/2}}{\xi_{zj+1/2}} \left(\frac{9}{8} (P_{i,j+1} - P_{i,j}) - \frac{1}{24} (P_{i,j+2} - P_{i,j-1}) \right) \right. \right. \\
 & - \left. \frac{b_{i,j-1/2}}{\xi_{zj-1/2}} \left(\frac{9}{8} (P_{i,j} - P_{i,j-1}) - \frac{1}{24} (P_{i,j+1} - P_{i,j-2}) \right) \right] \\
 & - \frac{1}{24} \left[\frac{b_{i,j+3/2}}{\xi_{zj+3/2}} \left(\frac{9}{8} (P_{i,j+2} - P_{i,j+1}) - \frac{1}{24} (P_{i,j+3} - P_{i,j}) \right) \right. \\
 & - \left. \left. \frac{b_{i,j-3/2}}{\xi_{zj-3/2}} \left(\frac{9}{8} (P_{i,j-1} - P_{i,j-2}) - \frac{1}{24} (P_{i,j} - P_{i,j-3}) \right) \right] \right\} + S_{i,j}.
 \end{aligned} \tag{24}$$

The pressure acceleration term $\omega^2/K(x, z)$ can also be averaged over the different nodes of the FD stencil as for the mixed-grid strategy. In this case eq. (24) becomes:

$$\begin{aligned}
 a_{\text{stg}} \frac{-\omega^2}{K_{i,j}} P_{i,j} + c_{\text{stg}} \left(\frac{-\omega^2}{K_{i+1,j}} P_{i+1,j} + \frac{-\omega^2}{K_{i-1,j}} P_{i-1,j} + \frac{-\omega^2}{K_{i,j+1}} P_{i,j+1} + \frac{-\omega^2}{K_{i,j-1}} P_{i,j-1} \right) \\
 + d_{\text{stg}} \left(\frac{-\omega^2}{K_{i+2,j}} P_{i+2,j} + \frac{-\omega^2}{K_{i+2,j}} P_{i+2,j} + \frac{-\omega^2}{K_{i,j-2}} P_{i,j-2} + \frac{-\omega^2}{K_{i,j+2}} P_{i,j+2} \right) \\
 + e_{\text{stg}} \left(\frac{-\omega^2}{K_{i-3,j}} P_{i-3,j} + \frac{-\omega^2}{K_{i+3,j}} P_{i+3,j} + \frac{-\omega^2}{K_{i,j-3}} P_{i,j-3} + \frac{-\omega^2}{K_{i,j+3}} P_{i,j+3} \right) \\
 = \frac{1}{\Delta^2 \xi_i} \left\{ \frac{9}{8} \left[\frac{b_{i+1/2,j}}{\xi_{xi+1/2}} \left(\frac{9}{8} (P_{i+1,j} - P_{i,j}) - \frac{1}{24} (P_{i+2,j} - P_{i-1,j}) \right) \right. \right. \\
 - \frac{b_{i-1/2,j}}{\xi_{xi-1/2}} \left(\frac{9}{8} (P_{i,j} - P_{i-1,j}) - \frac{1}{24} (P_{i+1,j} - P_{i-2,j}) \right) \left. \right] \\
 - \frac{1}{24} \left[\frac{b_{i+3/2,j}}{\xi_{xi+3/2}} \left(\frac{9}{8} (P_{i+2,j} - P_{i+1,j}) - \frac{1}{24} (P_{i+3,j} - P_{i,j}) \right) \right. \\
 - \left. \frac{b_{i-3/2,j}}{\xi_{xi-3/2}} \left(\frac{9}{8} (P_{i-1,j} - P_{i-2,j}) - \frac{1}{24} (P_{i,j} - P_{i-3,j}) \right) \right] \left. \right\} \\
 + \frac{1}{\Delta^2 \xi_j} \left\{ \frac{9}{8} \left[\frac{1}{\xi_{zj+1/2} \rho_{i,j+1/2}} \left(\frac{9}{8} (P_{i,j+1} - P_{i,j}) - \frac{1}{24} (P_{i,j+2} - P_{i,j-1}) \right) \right. \right. \\
 - \frac{b_{i,j-1/2}}{\xi_{zj-1/2}} \left(\frac{9}{8} (P_{i,j} - P_{i,j-1}) - \frac{1}{24} (P_{i,j+1} - P_{i,j-2}) \right) \left. \right] \\
 - \frac{1}{24} \left[\frac{b_{i,j+3/2}}{\xi_{zj+3/2}} \left(\frac{9}{8} (P_{i,j+2} - P_{i,j+1}) - \frac{1}{24} (P_{i,j+3} - P_{i,j}) \right) \right. \\
 - \left. \frac{b_{i,j-3/2}}{\xi_{zj-3/2}} \left(\frac{9}{8} (P_{i,j-1} - P_{i,j-2}) - \frac{1}{24} (P_{i,j} - P_{i,j-3}) \right) \right] \left. \right\} + S_{i,j},
 \end{aligned} \tag{25}$$

where $e_{\text{stg}} = [(1 - a_{\text{stg}})/4] - c_{\text{stg}} - d_{\text{stg}}$. The coefficients a_{stg} , c_{stg} and d_{stg} were computed such that the phase velocity dispersion is minimized in a least-square sense, following the approach used by Jo *et al.* (1996) and Štekl & Pratt (1998). The final coefficients that we obtained are $a_{\text{stg}} = 0.788614$, $b_{\text{stg}} = 7.92484 \times 10^{-2}$ and $c_{\text{stg}} = -3.22465 \times 10^{-2}$.

Let us underline that the averaging procedure is not essential to the unrotated staggered-grid numerical scheme. This is supported by the time-domain modelling shown in Fig. 2(a) which showed that the correct pressure field was computed at the staggered-grid nodes for a point source excited at one single grid node (i.e. without any smoothing of the source spatial distribution). In contrast, the erroneous pressure field is computed by the rotated numerical scheme when a point source is excited at one single grid node (Fig. 2b). This suggests that

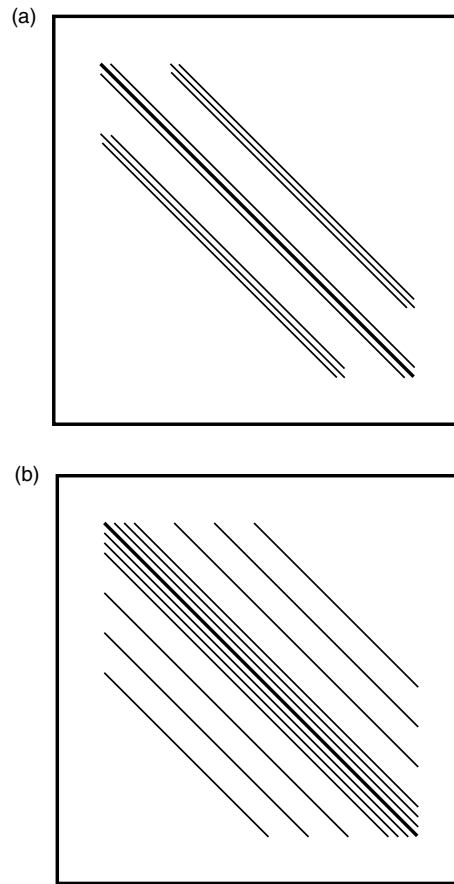


Figure 10. Illustration of the structure of the complex impedance matrix. Note that only the real part is shown. In (a) we display the result from the grid rotation approach. The matrix contains $(nx \times nz)^2$ elements from which $9 \times nx \times nz$ are non-zero. In (b) we plot the matrix structure that results from a fourth-order staggered-grid discretization of the first-order hyperbolic acoustic wave equation, reformulated to the parsimonious second-order hyperbolic equation. The matrix contains $(nx \times nz)^2$ elements from which $13 \times nx \times nz$ are non-zero. Note that in both (a) and (b) the main diagonal is plotted with a thicker line.

any numerical scheme involving the rotated-grid strategy (i.e. either the rotated staggered-grid or the mixed-grid strategies) requires some smoothing procedure such as the acceleration averaging technique or smoothing of the source spatial distribution.

In the time domain, acceleration averaging leads to an implicit formulation of the time integration, which has only been considered by few authors (e.g. Mufti 1985) in seismology. The main drawback is the induced matrix inversion, which may limit the size of the domain to be considered. One advantage is the possibility to select a coarser time stepping, which could be critical when different grid sizes are considered.

In the frequency domain, the matrix inversion is required in any case, and consequently the averaging procedure can be performed at nearly no additional cost and should therefore be selected even for this staggered-grid formulation.

4 GRID DISPERSION ANALYSIS

In this section, numerical precision of the fourth-order staggered-grid stencil is investigated for both the wavelength content and azimuthal variation. Furthermore, the staggered-grid approach is compared with the results obtained by Jo *et al.* (1996) for the mixed-grid approach. In Figs 5 and 6, we show dispersion curves for relative phase and group velocity for both the mixed-grid stencil and the fourth-order staggered-grid stencil, for plane wave propagation angles ranging from 0° to 45° . The number of gridpoints per wavelength is defined by $1/G$ (G is the number of gridpoints per wavelength). In Fig. 6, we used non-optimized fourth-order staggered-grid derivative approximations for the stencil and no averaging of the pressure acceleration term as done by Levander (1988).

From Figs 5 and 6 we find that the mixed-grid stencil shows less dispersive wave propagation for the same number of grid nodes per shortest wavelength compared with the staggered-grid stencil. This is true for both phase and group velocity dispersion curves.

A partly similar optimization strategy, first introduced for FDTD modelling by Holberg (1987), can be applied to the staggered-grid approach (Arntsen *et al.* 1998). In their approach, coefficients describing classical staggered derivative operator coefficients are replaced by optimized staggered operator coefficients that are obtained through a dispersion relation minimization technique. The fourth-order staggered-grid operator coefficients ($\alpha_1 = 9/8$ and $\alpha_2 = -1/24$) were replaced by $\alpha_1 = 1.13824281853071$ and $\alpha_2 = -4.64142728435701 \times 10^{-2}$. An example of the staggered-grid dispersion curve optimization is shown in Fig. 7. Both phase and group velocity dispersion curves are slightly improved when using optimized coefficients.

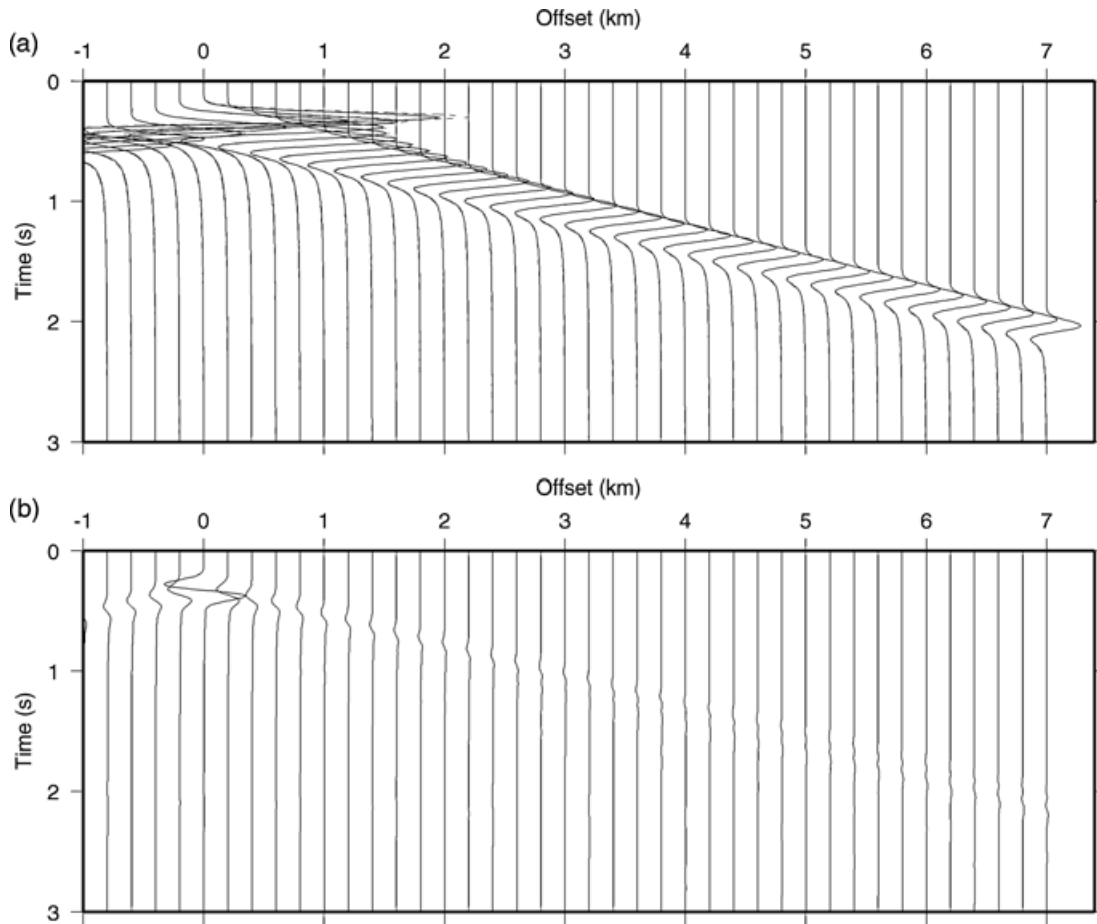


Figure 11. (a) Comparison of time-domain seismograms computed with the mixed-grid operator frequency-domain method (dashed line) and an analytical solution (solid line). (b) Difference between the two sets of seismograms.

Finally, we compute the dispersion curves for the fourth-order staggered-grid operator using the coefficients of Holberg (1987) and Levander (1988), combined with the averaging of the pressure acceleration term (eq. 25). The averaging coefficients that we computed for the optimized stencil are $a_{\text{stg}} = 0.817876$, $c_{\text{stg}} = 7.04578 \times 10^{-2}$ and $d_{\text{stg}} = -3.10661 \times 10^{-2}$. When using averaging of the pressure acceleration term we obtain a significant improvement of the phase velocity dispersion curve, both in terms of numerical dispersion and numerical anisotropy (Figs 8 and 9). The accuracy of the fourth-order staggered-grid operator using optimized coefficients combined with mass averaging is slightly better than the mixed-grid stencil. For $1/G$ ranging between 0 and 0.3, the maximum error for the phase velocity is 0.3 per cent and 1.2 per cent for the fourth-order staggered-grid and mixed-grid formulations respectively. Note, however, that the group velocity dispersion properties have been degraded by the mass term averaging (compare Figs 7, 8, and 9). Nevertheless, we are usually concerned by the modelling of non-dispersive waves. Therefore we considered that the phase velocity dispersion is the most significant criterion to assess the accuracy of a FD stencil (as suggested by the fact that only the phase velocity dispersion is minimized in the approach developed by Jo *et al.* 1996; Štekl & Pratt 1998).

In Appendix B, we demonstrate that the staggered-grid strategy exactly determines relative phase velocity v_{ph}/v and group velocity equal to 1 under the assumption of small propagation angles for an infinitely fine medium discretization ($v_{\text{ph}}/v = v_{\text{gr}}/v = 1$ for $1/G \Rightarrow 0$).

The mixed-grid approach obtains approximately similar results for numerical phase and group velocity ($v_{\text{ph}}/v \approx v_{\text{gr}}/v \approx 1$), because the numerical combination of the rotated grids (and the subsequent optimization of the numerical dispersion) shifts the dispersion curves. Indeed, the dispersion curves are better aligned to the ideal relative medium velocity for higher $1/G$ ratios (coarser discretization) while, at the same time, the accuracy for lower $1/G$ ratios is altered. In Fig. 6, this is observed from relative velocity values at $1/G \rightarrow 0$.

It is remarkable that the grid rotation preserves the very compact numerical stencil geometry while including the maximum amount of existing information in the surroundings of the centre point—a clear advantage for numerical FD modelling in 2-D with mixed grids.

5 SOLUTIONS FOR THE MATRIX EQUATION

These discrete frequency-domain wave equations (eqs 18 and 25) are recast into a matrix-type equation of the form:

$$\mathbf{M} \cdot \mathbf{p} = \mathbf{s}, \quad (26)$$

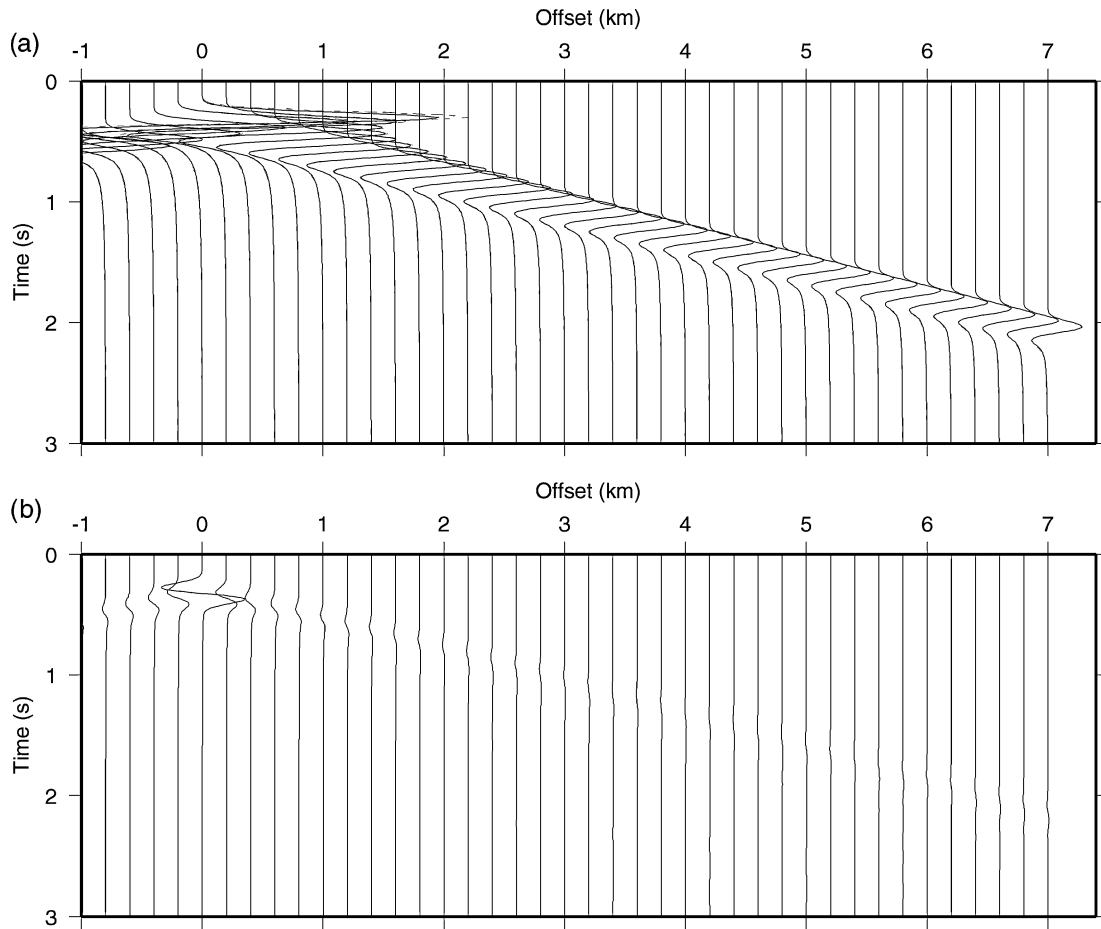


Figure 12. (a) Comparison of time-domain seismograms computed with the fourth-order staggered-grid frequency-domain method (dashed line) and an analytical solution (solid line). (b) Difference between the two sets of seismograms.

where \mathbf{M} is the so-called impedance matrix, \mathbf{p} is the pressure wavefield (desired solution) and \mathbf{s} is the source function. The matrix \mathbf{M} is complex-valued and depends on the physical model parameters: the density ρ , the bulk modulus K , and the angular frequency ω .

We compute wavefield solutions for each source position and each frequency component by solving the corresponding matrix equation (eq. 26) through an optimized minimum-order scheme developed by Davis & Duff (1997). The so-called UMFPAK solver combines a matrix pre-ordering strategy, that limits the numerical fill-in during the \mathbf{LU} decomposition, with an unsymmetric-pattern multifrontal factorization scheme. The multifrontal approach decomposes the initial matrix \mathbf{M} into a set of frontal submatrices, which allows the implementation of optimized pivot strategies that stabilize and accelerate the matrix factorization process.

For each frequency component, the complex matrix can be constructed and is factorized into its \mathbf{LU} factors. Pressure wavefield solutions for each source position and frequency component are computed separately. Clearly, the \mathbf{LU} decomposition needs to be computed only once for each frequency component, making this approach very appealing especially for multisource experiments (Pratt & Worthington 1990).

For example, the complex impedance matrix construction and subsequent \mathbf{LU} factorization for one frequency component f_j requires 98 per cent CPU time (10 per cent matrix construction + 88 per cent matrix factorization) while the solving phase ($\mathbf{LU}_{f_j} \cdot \mathbf{p}_{f_j} = \mathbf{s}_{f_j}^i$) for one source position \mathbf{s}^i only needs 2 per cent CPU time. Note that if a simple band-solver were to have been used for the matrix decomposition, the number of non-zero coefficients in the \mathbf{LU} factors would be significantly increased and, therefore, solving phase computations would be much slower. Only when highly optimized matrix factorization methods are employed, such as multifrontal methods or nested dissection (Štekl & Pratt 1998), does the storage and operation count reduce dramatically.

In the case of the mixed-grid stencil, the full matrix \mathbf{M} contains $(nx \times nz)^2$ elements of which $(9 \times nx \times nz)$ are different from zero. The non-zero elements are distributed on the diagonal and two adjacent bands. The bandwidth is approximately $2nz + 1$. The structure of the impedance matrix is illustrated in Fig. 10(a). In the case of fourth-order derivative approximations, the staggered-grid discretization gives a matrix \mathbf{M} that contains $(nx \times nz)^2$ elements from which $13 \times nx \times nz$ are non-zero (Fig. 3). The elements are distributed along the main diagonal (seven coefficients) and six adjacent parallel bands. The structure of the matrix is shown in Fig. 10(b). The bandwidth of the matrix is $6nz$, which is approximately three times larger than the matrix bandwidth resulting from the mixed-grid approach. The matrix appearing in the first-order PML formulation increases the number of non-zero coefficients for a given model configuration, since 13 points instead of nine

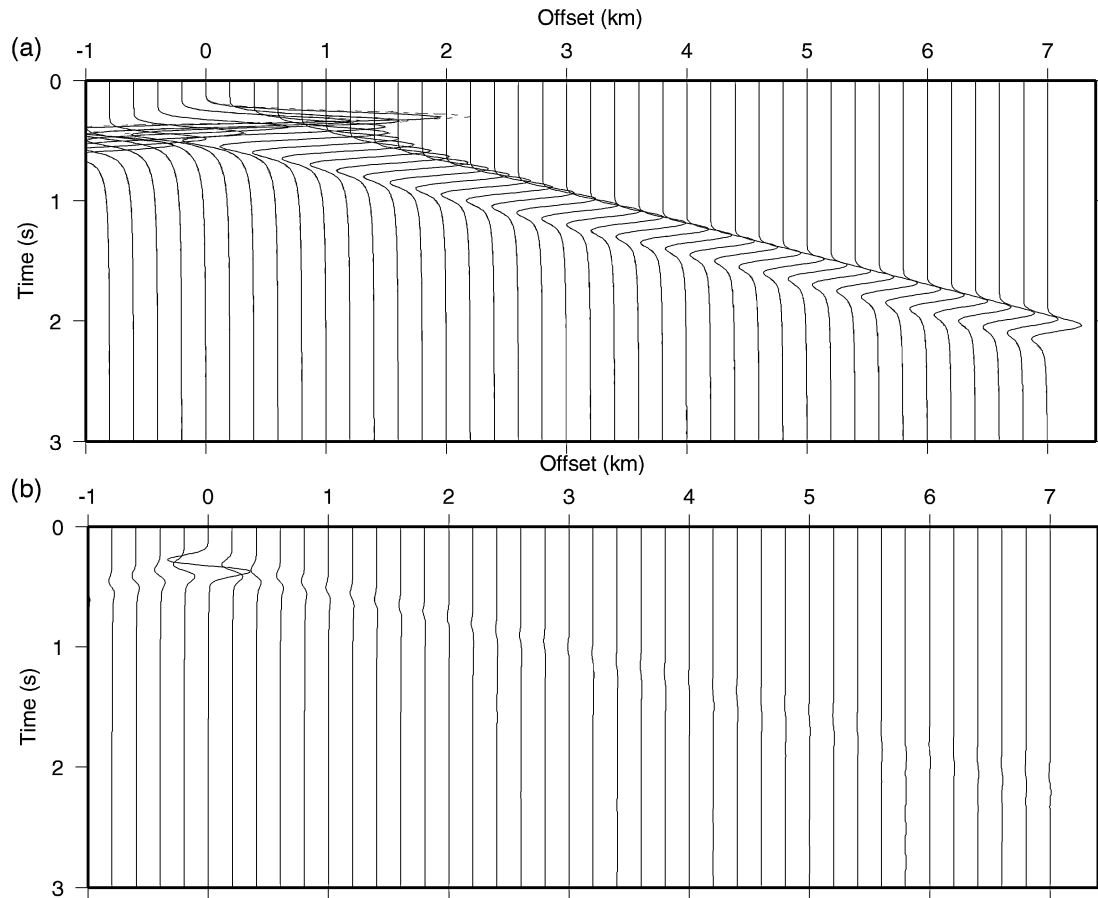


Figure 13. (a) Comparison of time-domain seismograms computed with the fourth-order staggered-grid frequency-domain method including acceleration averaging (dashed line) and an analytical solution (solid line). (b) Difference between the two sets of seismograms.

points are used for the derivative approximations. Therefore, increasing the matrix bandwidth and number of non-zero coefficients results in higher memory demands for the matrix ordering scheme.

The matrix characteristics such as the bandwidth, the number and the actual value of non-zero matrix coefficients are the key elements that control the performance of the **LU** factorization procedure. For example, if a simple band-ordering solver is used, then the entire matrix bandwidth that initially holds only zero coefficients will be filled-in with non-zeros. Even though we apply a sophisticated ordering scheme, we expect the staggered-grid stencil construction to be less efficient in terms of CPU time, because of the spatial extension mentioned in the previous paragraph. We shall see this with numerical examples below.

6 NUMERICAL EXAMPLES

6.1 The homogeneous full space model

We first compare the mixed-grid approach with the fourth-order staggered-grid approach for an acoustic wave simulation in a 2-D homogeneous medium. The velocity is 4000 m s^{-1} and the density is 2500 kg m^{-3} . The vertical and horizontal dimensions of the model are 4000 m and 8000 m, respectively. The spatial sampling is 40 m, which corresponds approximately to eight points per shortest wavelength. The source is an impulsional point source located at ($z = 500 \text{ m}$, $x = 1000 \text{ m}$). The source is excited at one single gridpoint (i.e. the vector \mathbf{s} in eq. (26) has only one non-zero element at the location of the impulsional source). For the temporal source excitation, we used a Gaussian derivative $S(t) = -2\alpha(t-t_0)e^{-\alpha(t-t_0)^2}$ with $\alpha = 200$, $t_0 = 0.3 \text{ s}$. The central and maximum frequencies of the source are approximately 3.15 and 12 Hz respectively. The minimum wavelength is 200 m. Forty receivers are spread out over the whole model at a constant depth of 400 m and with a horizontal spacing between receivers of 200 m.

We compute frequency-domain solutions for 308 frequency components, spanning a range from 0 to 15 Hz. The inverse Fourier transform is applied to the frequency-domain solutions to obtain time-domain seismograms. The maximum time of the seismograms is set to 20 s, for accurate frequency sampling. For both approaches, we set PML absorbing boundary conditions on all edges of the model using the same damping conditions throughout. In Fig. 11 we show the comparison between seismograms computed for the mixed-grid strategy (dashed line)

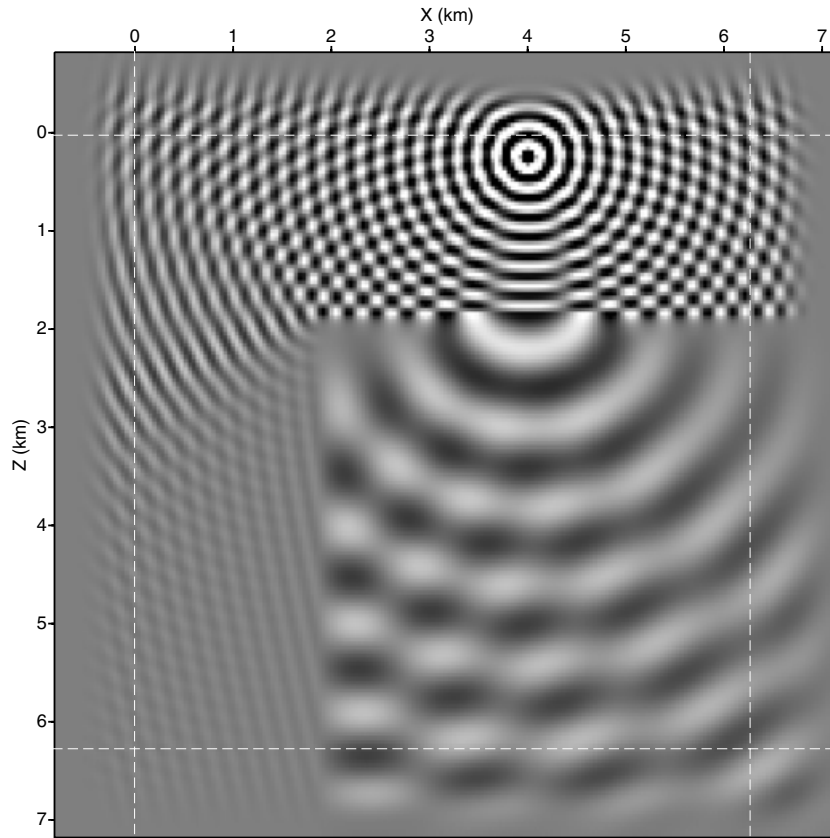


Figure 14. 10 Hz monochromatic wavefield computed in the corner-edge model. The horizontal interface is at a depth of 1.88 km. The horizontal and vertical interface are at a distance and depth of 1.88 km, respectively. The white dashed line delineates the PML layers. The wavefield is computed using the fourth-order staggered-grid frequency-domain method.

and the analytical solution (solid line). Seismograms are plotted with their true amplitude (no amplitude normalization was applied to the analytical and FD seismograms).

The overall agreement is excellent except for the receiver located just above the source, where the amplitude of the FD seismogram is overestimated. This mismatch can be mitigated by smoothing the spatial distribution of the impulsional source, although accuracy of the FD seismograms is slightly degraded at larger offsets (not shown).

The same comparison is shown in Figs 12 and 13 but for FD seismograms computed with the fourth-order staggered-grid stencil, with and without averaging of the mass acceleration term respectively. The coefficients of Levander in the FD stencil were used ($\alpha_1 = 9/8$ and $\alpha_2 = -1/24$). The fit with the analytical solution is slightly better than for the mixed-grid operator FD seismograms.

As expected, the computational time required by the mixed-grid formulation is much lower than for the staggered-grid stencil. The time required to produce the time-domain seismograms is 45 min and 5 h for the mixed-grid operator and the fourth-order staggered-grid simulations respectively. The modelling was carried out on a Linux PC with 512 Mbytes of RAM.

6.2 The corner edge model

The corner edge model combines two homogeneous media separated by a horizontal and a vertical interface making a corner (see Fig. 14). The velocity and density in the two spaces are 2000 m s^{-1} , 8000 m s^{-1} and 2000 kg m^{-3} , 2500 kg m^{-3} , respectively. The dimension of the model is $6400 \text{ m} \times 6400 \text{ m}$ and is discretized with a mesh spacing of 40 m (equal to around four points per shortest wavelength). All four edges of the model are treated with PML absorbing boundary conditions, where the layer size is set to 20 gridpoints. Therefore, the overall grid has 200×200 gridpoints. As for the homogeneous case, the maximum time of the seismograms is set to 20 s for accurate frequency sampling. This leads to 308 frequencies in the 0–15 Hz frequency range.

The source position is at ($z = 240 \text{ m}$, $x = 4000 \text{ m}$). We use the same source as for the homogeneous model comparison. The seismograms are recorded by 81 receiver positions aligned horizontally over the whole model, at a depth of 160 m.

We compare time-domain seismograms computed with a $\mathcal{O}(\Delta t^2, \Delta x^4)$ time-space staggered-grid method (see Operto *et al.* (2002) for examples of application of this code in the case of the *SH*-wave equation) and the frequency-domain methods based on the mixed-grid and fourth-order staggered-grid stencils. In Figs 15, 16 and 17, we show the comparison between the seismograms computed with the time-space method and the frequency-domain method. For the latter simulations we apply the mixed-grid stencil and the fourth-order staggered-grid

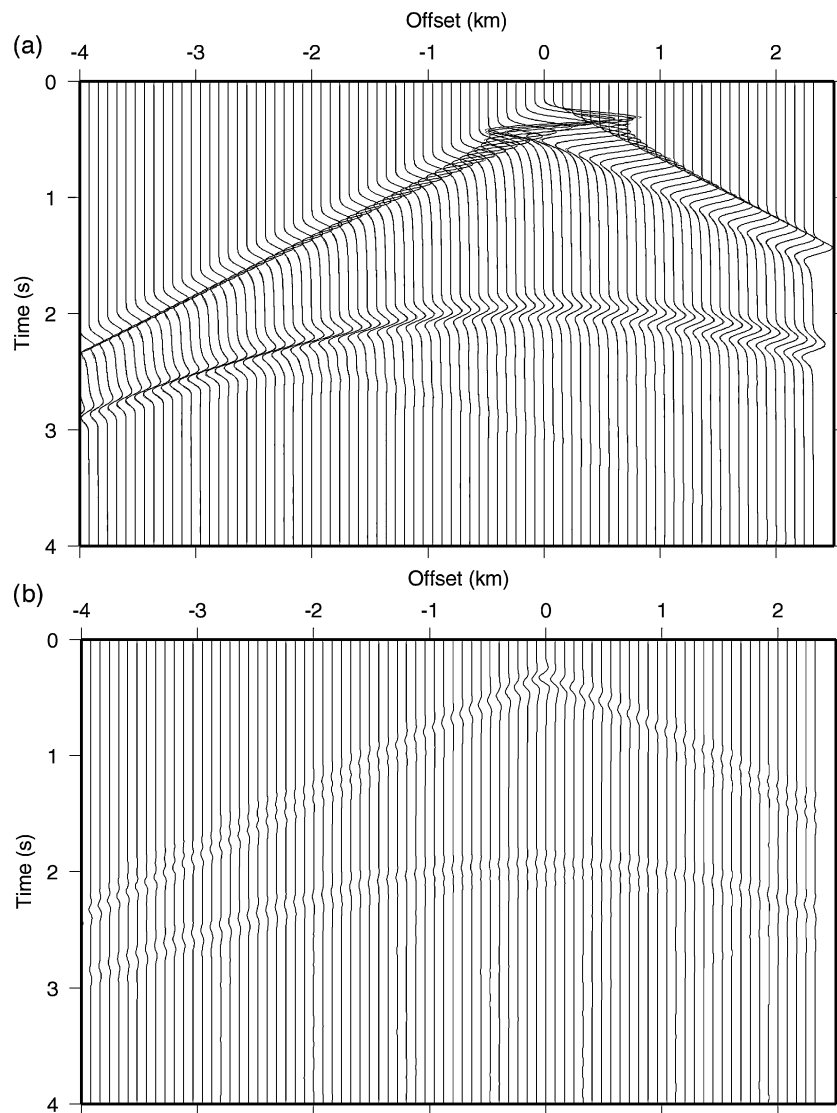


Figure 15. (a) Comparison of a finite-difference time-domain fourth-order staggered-grid solution (solid line) and the finite-difference frequency-domain rotated-grid operator solution (dashed line) for the 2-D corner edge simulation. (b) Difference between the two sets of seismograms.

stencil with and without acceleration averaging respectively. We observe on the seismograms the direct wave, a strong reflection from the horizontal edge, and a weak diffraction excited by the corner.

The three frequency-domain solutions agree well with the time-domain method solution. No amplitude normalization is applied to the seismograms. We note that the residual between the solutions computed with the time-domain and the mixed-grid operator methods exhibit some dispersion. This illustrates that the two stencils rely on different approaches. On the contrary, residuals between the time-domain and the staggered-grid frequency-domain methods do not exhibit such dispersion, which is easily explained by the fact that the spatial stencils are identical in both methods.

The time required to produce the time-domain seismograms is 51 min and 7.5 h for the mixed-grid operator and the fourth-order staggered-grid simulations respectively. The modelling was carried out on a Linux PC with 512 Mbytes of RAM.

7 PERSPECTIVES AND CONCLUSION

We present two staggered-grid strategies for FDFD acoustic wave propagation modelling in 2-D media. The two approaches discretize the first derivative operator on the Cartesian coordinate system and the 45° rotated system, using a second-order centred FD stencil. The second approach is the frequency-domain analogue of the time-domain approach developed by Saenger *et al.* (2000) for the elastic wave equation. Staggered-grid approaches discretize the wave equation written as a first-order hyperbolic system of equations including PML absorbing boundary conditions. Parsimonious elimination followed by reinjection leads to a second-order hyperbolic equation which allows minimal numerical implementation schemes for both approaches. The two staggered-grid geometries share the same nodes for the pressure field, while acoustic equivalents of the particle velocities are distributed on different nodes.

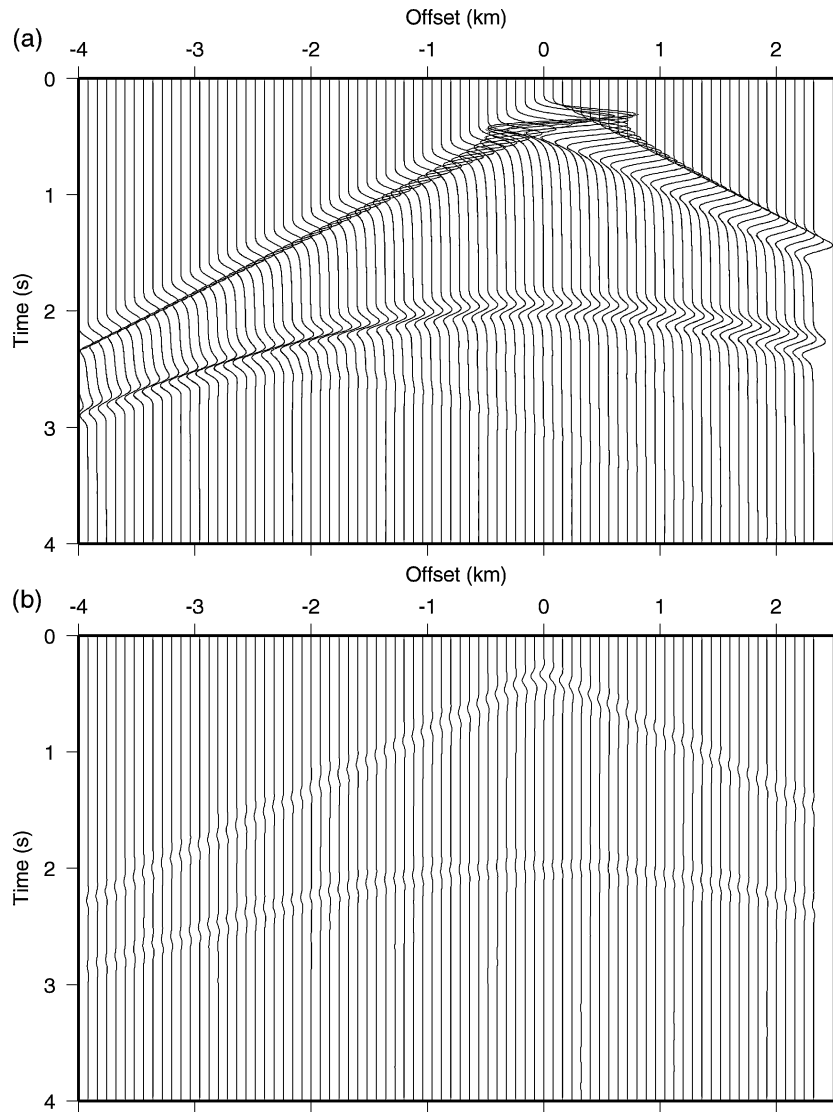


Figure 16. (a) Comparison of a finite-difference time-domain fourth-order staggered-grid solution (solid line) and the finite-difference frequency-domain fourth-order staggered-grid solution (dashed line) for the 2-D corner edge simulation. (b) Difference between the two sets of seismograms.

We show that the staggered-grid stencil on the Cartesian coordinate system is identical to the centred five-point stencil strategy used by Pratt & Worthington (1990), when terms due to the PML absorbing boundary conditions are neglected.

We extend the staggered-grid method to fourth-order accurate FD approximation of the first derivative on the Cartesian coordinate system. The fourth-order staggered-grid method is compared with the mixed-grid method. The mixed-grid method linearly combines the two second-order staggered-grid stencils on the Cartesian coordinate system and the rotated system. The mixed-grid method is accurate only if an averaging of the acceleration term is incorporated in the stencil. This averaging strengthens the coupling between the two staggered-grid stencils of different accuracy and geometry.

Numerical dispersion is investigated for the staggered-grid and mixed-grid stencils. For the mixed-grid discretization, both phase and group velocity show less numerical dispersion than for the staggered-grid discretization. Since the combination of the stencils in the mixed-grid method requires some dispersion relation optimization technique, we apply an analogous optimization to the staggered-grid approach in order to enhance the approximation of the first-derivative operator.

Though numerical dispersion decreases when compared with the standard fourth-order staggered-grid approximation, it is still not competitive with respect to the mixed-grid formulation. In the end, we add an acceleration term averaging to the optimized staggered-grid stencil. In this case, the staggered-grid stencil turns out to be slightly superior to the mixed-grid stencil with respect to the phase velocity dispersion.

The CPU efficiency of the two discretization approaches is controlled by the matrix factorization scheme and, therefore, by the compactness of the discrete stencil geometry. Fewer surrounding points involved in the stencil construction are more favourable. Since the staggered-grid

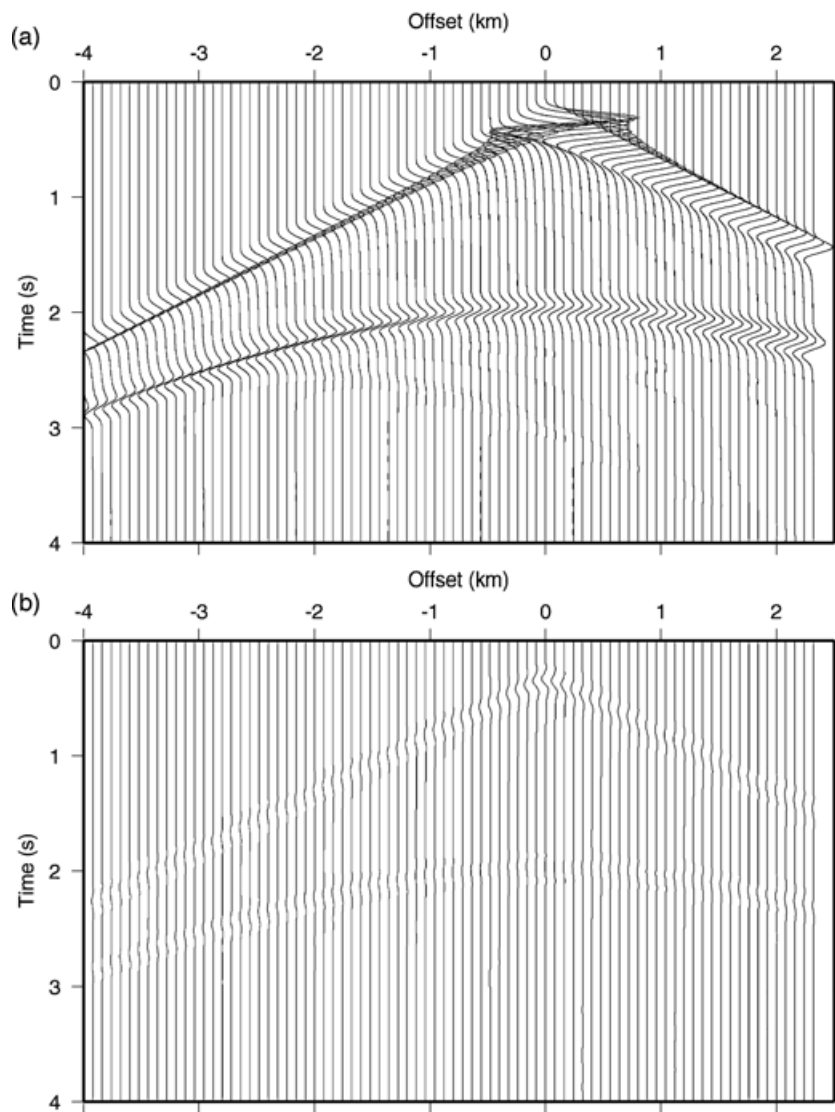


Figure 17. (a) Comparison of a finite-difference time-domain fourth-order staggered-grid solution (solid line) and the finite-difference frequency-domain fourth-order staggered-grid, including acceleration averaging, solution (dashed line) for the 2-D corner edge simulation. (b) Difference between the two sets of seismograms.

stencil for fourth-order approximations holds 13 gridpoints instead of nine points for the mixed-grid stencil, the memory requirements and CPU floating point operations for matrix factorizations significantly increase.

Altogether, the mixed-grid strategy shows clearly superior results for 2-D FDFD modelling in terms of memory requirements and CPU efficiency. In view of the performance of the mixed-grid approach the question arises as to why, in FDTD modelling, the staggered-grid approach predominates while in FDFD modelling the rotated-grid approach is preferred. The main reason seems to be that in the latter case the necessary mass acceleration averaging (i.e. antilumping of the mass matrix) implies matrix inversion at each step of the integration, from the time t till the time $t + dt$. In FDTD modelling, the compactness of the discrete stencil plays a less important role since no matrix factorization is computed. Moreover, the mixed-grid approach cannot be implemented in the time domain with a first-order hyperbolic formulation based on staggered grids because of the conflicting geometry of the two stencils. Only a non-staggered-grid approach can be implemented, which requires a decrease of the mesh stepping by 2.

The combination of rotated grids and staggered grids has already been addressed by Saenger *et al.* (2000). However, in their approach only the derivative approximations are described on rotated axis while the wave equation is left untouched. They obtained superior simulation results for wave diffractions by a crack, but did not address a higher-order scheme in order to enhance the numerical performance of the FDTD scheme. Therefore, we propose that the compact and optimized rotated-grid stencil should be investigated for FDTD modelling in complex heterogeneous media. This work is in progress.

We present and compare different techniques for the construction of finite-difference schemes. We show that for acoustic wave simulation in the frequency domain, the mixed-grid scheme leads to the most adapted stencil due to its CPU efficiency. During this investigation, we

have shown the link between the mixed-grid method and the staggered-grid method. As an additional result, a new and more accurate PML absorbing boundary condition arise for the mixed-grid method.

ACKNOWLEDGMENTS

We are thankful to D. Rodrigues for providing us with the fourth-order staggered-grid stencil optimization coefficients. We would like to thank P. Amestoy for assistance with the optimized minimum degree ordering scheme. Support from IDRIS (Institut du Développement et des Ressources en Informatique Scientifique) through project 21560 is acknowledged. The research leading to this paper was partly founded by DASE/CEA through the PROSIS3D group. The reviews provided by G. Pratt and K. Olsen were extremely helpful and led to significant improvements in the quality of the manuscript. This paper is contribution no 643 from UMR Geosciences Azur, CNRS, France.

REFERENCES

- Arntsen, B., Nebel, A. & Amundsen, L., 1998. Visco-acoustic finite-difference modeling in the frequency domain, *J. Seism. Explor.*, **7**, 45–64.
- Berenger, J.P., 1994. A perfectly matched layer for the absorption of electromagnetic waves, *J. Comput. Phys.*, **114**, 185–200.
- Boore, D.M., 1972. Finite-difference methods for seismic wave propagation in heterogeneous materials, in *Methods in Computational Physics*, eds Bolt, B.A., Alder, B., Frenbach, S., Rotemberg, M., **11**, pp. 1–36, Academic Press, New York.
- Clayton, R. & Engquist, B., 1977. Absorbing boundary conditions for acoustic and elastic wave equations, *Bull. seism. Soc. Am.*, **67**, 1529–1540.
- Cruz-Atienza, V.M. & Virieux, J., 2003. Dynamic rupture simulation of bent faults with a finite difference approach, *Geophys. J. Int.*, in press.
- Dablain, M.A., 1986. The application of higher order differencing to the scalar wave equation, *Geophysics*, **51**, 54–66.
- Davis, T.A. & Duff, I.S., 1997. An unsymmetric-pattern multifrontal method for LU factorization, *SIAM J. Sci. Stat. Comput.*, **18**, 140–158.
- Dessa, J.X., 2001. Modélisation et inversion de la forme d'onde en domaine fréquentiel: applications à la tomographie multi-offsets, *PhD thesis*, University Paris-Sud.
- Graves, R.W., 1996. Simulating seismic wave propagation in 3d elastic media using staggered grid finite differences, *Bull. seism. Soc. Am.*, **86**, 1091–1106.
- Holberg, O., 1987. Computational aspects of the choice of operator and sampling interval for numerical differentiation in large-scale simulation of wave phenomena, *Geophys. Prospect.*, **35**, 629–655.
- Hustedt, B., 2002. Propagation des ondes: approches espace et ondelettes, *PhD thesis*, University of Nice-Sophia-Antipolis.
- Jo, C.H., Shin, C.S. & Suh, J.H., 1996. An optimal 9 point, finite difference, frequency-space, 2-D wave extrapolator, *Geophysics*, **61**, 529–537.
- Kelly, K.R., Ward, R.W., Treitel, S. & Alford, R.M., 1976. Synthetic seismograms: a finite difference approach, *Geophysics*, **41**, 2–27.
- Levander, A.R., 1988. Fourth-order finite-difference P-SV seismograms, *Geophysics*, **53**, 1425–1436.
- Luo, Y. & Schuster, G., 1990. Parsimonious staggered grid finite differencing of the wave equation, *Geophys. Res. Lett.*, **17**(2), 155–158.
- Madariaga, R., 1976. Dynamics of an expanding circular fault, *Bull. seism. Soc. Am.*, **73**, 765–780.
- Mufti, I.R., 1985. Seismic modeling in the implicit mode, *Geophys. Prospect.*, **33**, 619–656.
- Nougier, J.P., 1989. *Méthodes de Calcul Numérique*, Masson, Paris.
- Operto, S., Virieux, J., Hustedt, B. & Malfanti, F., 2002. Adaptive wavelet-based finite-difference modelling of SH-wave propagation, *Geophys. J. Int.*, **148**(3), 477–499.
- Pratt, R.G., 1990. Inverse theory applied to multi-source cross-hole tomography, part 2: Elastic wave-equation method, *Geophys. Prospect.*, **38**, 311–329.
- Pratt, R.G. & Worthington, M.H., 1990. Inverse theory applied to multi-source cross-hole tomography, part 1: Acoustic wave-equation method, *Geophys. Prospect.*, **38**, 287–310.
- Saenger, E.H., Gold, N. & Shapiro, A., 2000. Modeling the propagation of elastic waves using a modified finite-difference grid, *Wave Motion*, **31**, 77–92.
- Shin, C. & Sohn, H., 1998. A frequency-space 2-d scalar wave extrapolator using extended 25-point finite-difference operator, *Geophysics*, **63**, 289–296.
- Virieux, J., 1984. SH wave propagation in heterogeneous media, velocity-stress finite difference method, *Geophysics*, **49**, 1259–1266.
- Virieux, J., 1986. P-SV wave propagation in heterogeneous media, velocity-stress finite difference method, *Geophysics*, **51**, 889–901.
- Štekl, I., 1997. Frequency domain seismic forward modelling: a tool for waveform inversion, *PhD thesis*, Department of Geology, Royal School of Mines, Imperial College London.
- Štekl, I. & Pratt, R.G., 1998. Accurate viscoelastic modeling by frequency-domain finite differences using rotated operators, *Geophysics*, **63**(5), 1779–1794.
- Zhang, Y.-G. & Ballmann, J., 1997. Two techniques for the absorption of elastic waves using an artificial transition layer, *Wave Motion*, **25**, 15–33.
- Zienkiewicz, O.C. & Morgan, K., 1982. *Finite Elements and Approximation*, John Wiley, New York.

APPENDIX A: FOURTH-ORDER DISCRETIZATION OF THE WAVE EQUATION

We show the discretization procedure of the first-order hyperbolic system of equations using the fourth-order spatially staggered stencil. The procedure is similar to the one used for second-order derivative approximations on staggered grids. This formulation leads to a staggered-grid stencil that propagates pressure wavefield solutions with fourth-order accuracy.

We discretize eq. (21) using fourth-order staggered-grid geometry employed by Levander (1988):

$$\begin{aligned}
 \frac{\partial Q}{\partial x} &\approx \frac{1}{\Delta} \left(\frac{9}{8} (Q_{i+1/2,j} - Q_{i-1/2,j}) - \frac{1}{24} (Q_{i+3/2,j} - Q_{i-3/2,j}) \right) \\
 \frac{\partial R}{\partial x} &\approx \frac{1}{\Delta} \left(\frac{9}{8} (R_{i,j+1/2} - R_{i,j-1/2}) - \frac{1}{24} (R_{i,j+3/2} - R_{i,j-3/2}) \right) \\
 \frac{\partial P}{\partial x} &\approx \frac{1}{\Delta} \left(\frac{9}{8} (P_{i+1,j} - P_{i,j}) - \frac{1}{24} (P_{i+2,j} - P_{i-1,j}) \right) \\
 \frac{\partial P}{\partial z} &\approx \frac{1}{\Delta} \left(\frac{9}{8} (P_{i,j+1} - P_{i,j}) - \frac{1}{24} (P_{i,j+2} - P_{i,j-1}) \right),
 \end{aligned} \tag{A1}$$

where Δ is the mesh spacing in the uniform grid.

We obtain the following relations:

$$\begin{aligned}
 \frac{-i\omega\xi_{xi}}{K_{i,j}}P_{xi,j} &= \frac{1}{\Delta} \left(\frac{9}{8}(Q_{i+1/2,j} - Q_{i-1/2,j}) - \frac{1}{24}(Q_{i+3/2,j} - Q_{i-3/2,j}) \right) + S_{i,j} \\
 \frac{-i\omega\xi_{zi}}{K_{i,j}}P_{zi,j} &= \frac{1}{\Delta} \left(\frac{9}{8}(R_{i+1/2,j} - R_{i-1/2,j}) - \frac{1}{24}(R_{i+3/2,j} - R_{i-3/2,j}) \right) \\
 Q_{i+1/2,j} &= -\frac{1}{i\omega\xi_{i+1/2}\rho_{i+1/2,j}} \frac{1}{\Delta} \left(\frac{9}{8}(P_{i+1,j} - P_{i,j}) - \frac{1}{24}(P_{i+2,j} - P_{i-1,j}) \right) \\
 Q_{i-1/2,j} &= -\frac{1}{i\omega\xi_{i-1/2}\rho_{i-1/2,j}} \frac{1}{\Delta} \left(\frac{9}{8}(P_{i,j} - P_{i-1,j}) - \frac{1}{24}(P_{i+1,j} - P_{i-2,j}) \right) \\
 Q_{i+3/2,j} &= -\frac{1}{i\omega\xi_{i+3/2}\rho_{i+3/2,j}} \frac{1}{\Delta} \left(\frac{9}{8}(P_{i+2,j} - P_{i+1,j}) - \frac{1}{24}(P_{i+3,j} - P_{i,j}) \right) \\
 Q_{i-3/2,j} &= -\frac{1}{i\omega\xi_{i-3/2}\rho_{i-3/2,j}} \frac{1}{\Delta} \left(\frac{9}{8}(P_{i-1,j} - P_{i-2,j}) - \frac{1}{24}(P_{i,j} - P_{i-3,j}) \right) \\
 R_{i,j+1/2} &= -\frac{1}{i\omega\xi_{j+1/2}\rho_{i,j+1/2}} \frac{1}{\Delta} \left(\frac{9}{8}(P_{i,j+1} - P_{i,j}) - \frac{1}{24}(P_{i,j+2} - P_{i,j-1}) \right) \\
 R_{i,j-1/2} &= -\frac{1}{i\omega\xi_{j-1/2}\rho_{i,j-1/2}} \frac{1}{\Delta} \left(\frac{9}{8}(P_{i,j} - P_{i,j-1}) - \frac{1}{24}(P_{i,j+1} - P_{i,j-2}) \right) \\
 R_{i,j+3/2} &= -\frac{1}{i\omega\xi_{j+3/2}\rho_{i,j+3/2}} \frac{1}{\Delta} \left(\frac{9}{8}(P_{i,j+2} - P_{i,j+1}) - \frac{1}{24}(P_{i,j+3} - P_{i,j}) \right) \\
 R_{i,j-3/2} &= -\frac{1}{i\omega\xi_{j-3/2}\rho_{i,j-3/2}} \frac{1}{\Delta} \left(\frac{9}{8}(P_{i,j-1} - P_{i,j-2}) - \frac{1}{24}(P_{i,j} - P_{i,j-3}) \right), \tag{A2}
 \end{aligned}$$

where we use effective medium parameters and PML boundary conditions as before. We combine the equations and obtain for the pressure wavefield:

$$\begin{aligned}
 \frac{-\omega^2}{K_{i,j}}P_{i,j} &= \frac{1}{\Delta^2\xi_i} \left\{ \frac{9}{8} \left[\frac{1}{\xi_{xi+1/2}\rho_{i+1/2,j}} \left(\frac{9}{8}(P_{i+1,j} - P_{i,j}) - \frac{1}{24}(P_{i+2,j} - P_{i-1,j}) \right) \right. \right. \\
 &\quad \left. \left. - \frac{1}{\xi_{xi-1/2}\rho_{i-1/2,j}} \left(\frac{9}{8}(P_{i,j} - P_{i-1,j}) - \frac{1}{24}(P_{i+1,j} - P_{i-2,j}) \right) \right] \right. \\
 &\quad \left. - \frac{1}{24} \left[\frac{1}{\xi_{xi+3/2}\rho_{i+3/2,j}} \left(\frac{9}{8}(P_{i+2,j} - P_{i+1,j}) - \frac{1}{24}(P_{i+3,j} - P_{i,j}) \right) \right. \right. \\
 &\quad \left. \left. - \frac{1}{\xi_{xi-3/2}\rho_{i-3/2,j}} \left(\frac{9}{8}(P_{i-1,j} - P_{i-2,j}) - \frac{1}{24}(P_{i,j} - P_{i-3,j}) \right) \right] \right\} \\
 &+ \frac{1}{\Delta^2\xi_j} \left\{ \frac{9}{8} \left[\frac{1}{\xi_{zj+1/2}\rho_{i,j+1/2}} \left(\frac{9}{8}(P_{i,j+1} - P_{i,j}) - \frac{1}{24}(P_{i,j+2} - P_{i,j-1}) \right) \right. \right. \\
 &\quad \left. \left. - \frac{1}{\xi_{zj-1/2}\rho_{i,j-1/2}} \left(\frac{9}{8}(P_{i,j} - P_{i,j-1}) - \frac{1}{24}(P_{i,j+1} - P_{i,j-2}) \right) \right] \right. \\
 &\quad \left. - \frac{1}{24} \left[\frac{1}{\xi_{zj+3/2}\rho_{i,j+3/2}} \left(\frac{9}{8}(P_{i,j+2} - P_{i,j+1}) - \frac{1}{24}(P_{i,j+3} - P_{i,j}) \right) \right. \right. \\
 &\quad \left. \left. - \frac{1}{\xi_{zj-3/2}\rho_{i,j-3/2}} \left(\frac{9}{8}(P_{i,j-1} - P_{i,j-2}) - \frac{1}{24}(P_{i,j} - P_{i,j-3}) \right) \right] \right\} + S_{i,j}. \tag{A3}
 \end{aligned}$$

Finally, we write gridpoint contributions of the new staggered-grid stencil for fourth-order derivative approximations that are valid for the whole medium, including PML absorbing boundary conditions. We note that the staggered-grid approach results in a stencil that incorporates

13 grid nodes (see Fig. 3):

$$\begin{aligned}
C_1 &= \frac{\omega^2}{K_{i,j}} - \frac{1}{\Delta^2 \xi_i} \left[\frac{9}{8} \frac{9}{8} \left(\frac{1}{\xi_{i+1/2} \rho_{i+1/2,j}} + \frac{1}{\xi_{i-1/2} \rho_{i-1/2,j}} \right) \right. \\
&\quad \left. + \frac{1}{24} \frac{1}{24} \left(\frac{1}{\xi_{i+3/2} \rho_{i+3/2,j}} + \frac{1}{\xi_{i-3/2} \rho_{i-3/2,j}} \right) \right] \\
&\quad - \frac{1}{\Delta^2 \xi_j} \left[\frac{9}{8} \frac{9}{8} \left(\frac{1}{\xi_{j+1/2} \rho_{i,j+1/2}} + \frac{1}{\xi_{j-1/2} \rho_{i,j-1/2}} \right) \right. \\
&\quad \left. + \frac{1}{24} \frac{1}{24} \left(\frac{1}{\xi_{j+3/2} \rho_{i,j+3/2}} + \frac{1}{\xi_{j-3/2} \rho_{i,j-3/2}} \right) \right] \\
C_2 &= + \frac{1}{\Delta^2} \frac{1}{\xi_i} \left(\frac{9}{8} \frac{9}{8} \frac{1}{\xi_{i-1/2} \rho_{i-1/2,j}} + \frac{9}{8} \frac{1}{24} \frac{1}{\xi_{i+1/2} \rho_{i+1/2,j}} + \frac{1}{24} \frac{9}{8} \frac{1}{\xi_{i-3/2} \rho_{i-3/2,j}} \right) \\
C_3 &= + \frac{1}{\Delta^2} \frac{1}{\xi_i} \left(\frac{9}{8} \frac{9}{8} \frac{1}{\xi_{i+1/2} \rho_{i+1/2,j}} + \frac{9}{8} \frac{1}{24} \frac{1}{\xi_{i-1/2} \rho_{i-1/2,j}} + \frac{1}{24} \frac{9}{8} \frac{1}{\xi_{i+3/2} \rho_{i+3/2,j}} \right) \\
C_4 &= + \frac{1}{\Delta^2} \frac{1}{\xi_j} \left(\frac{9}{8} \frac{9}{8} \frac{1}{\xi_{j-1/2} \rho_{i,j-1/2}} + \frac{9}{8} \frac{1}{24} \frac{1}{\xi_{j+1/2} \rho_{i,j+1/2}} + \frac{1}{24} \frac{9}{8} \frac{1}{\xi_{j-3/2} \rho_{i,j-3/2}} \right) \\
C_5 &= + \frac{1}{\Delta^2} \frac{1}{\xi_j} \left(\frac{9}{8} \frac{9}{8} \frac{1}{\xi_{j+1/2} \rho_{i,j+1/2}} + \frac{9}{8} \frac{1}{24} \frac{1}{\xi_{j-1/2} \rho_{i,j-1/2}} + \frac{1}{24} \frac{9}{8} \frac{1}{\xi_{j+3/2} \rho_{i,j+3/2}} \right) \\
C_6 &= - \frac{1}{\Delta^2} \frac{1}{\xi_i} \left(\frac{9}{8} \frac{1}{24} \frac{1}{\xi_{i-1/2} \rho_{i-1/2,j}} + \frac{1}{24} \frac{9}{8} \frac{1}{\xi_{i-3/2} \rho_{i-3/2,j}} \right) \\
C_7 &= - \frac{1}{\Delta^2} \frac{1}{\xi_i} \left(\frac{9}{8} \frac{1}{24} \frac{1}{\xi_{i+1/2} \rho_{i+1/2,j}} + \frac{1}{24} \frac{9}{8} \frac{1}{\xi_{i+3/2} \rho_{i+3/2,j}} \right) \\
C_8 &= - \frac{1}{\Delta^2} \frac{1}{\xi_j} \left(\frac{9}{8} \frac{1}{24} \frac{1}{\xi_{j-1/2} \rho_{i,j-1/2}} + \frac{1}{24} \frac{9}{8} \frac{1}{\xi_{j-3/2} \rho_{i,j-3/2}} \right) \\
C_9 &= - \frac{1}{\Delta^2} \frac{1}{\xi_j} \left(\frac{9}{8} \frac{1}{24} \frac{1}{\xi_{j+1/2} \rho_{i,j+1/2}} + \frac{1}{24} \frac{9}{8} \frac{1}{\xi_{j+3/2} \rho_{i,j+3/2}} \right) \\
C_{10} &= + \frac{1}{\Delta^2} \frac{1}{\xi_i} \left(\frac{1}{24} \frac{1}{24} \frac{1}{\xi_{i-3/2} \rho_{i-3/2,j}} \right) \\
C_{11} &= + \frac{1}{\Delta^2} \frac{1}{\xi_i} \left(\frac{1}{24} \frac{1}{24} \frac{1}{\xi_{i+3/2} \rho_{i+3/2,j}} \right) \\
C_{12} &= + \frac{1}{\Delta^2} \frac{1}{\xi_j} \left(\frac{1}{24} \frac{1}{24} \frac{1}{\xi_{j-3/2} \rho_{i,j-3/2}} \right) \\
C_{13} &= + \frac{1}{\Delta^2} \frac{1}{\xi_j} \left(\frac{1}{24} \frac{1}{24} \frac{1}{\xi_{j+3/2} \rho_{i,j+3/2}} \right). \tag{A4}
\end{aligned}$$

APPENDIX B: DISPERSION ANALYSIS

We substitute a plane wave solution of the form $P = P_0 e^{-i(k_x x + k_z z)}$ into eq. (3) for the fourth-order staggered-grid stencil. We further assume $\Delta x = \Delta z = \Delta$ to be the uniform grid spacing in the x and the z directions. The propagation angle from the z -axis is denoted by θ , the spatial wavenumber by k , and the operator coefficients for the staggered derivative approximation by α_1 and α_2 (for example, $\alpha_1 = 9/8$ and $\alpha_1 = -1/24$ in the case of the fourth-order staggered-grid operator). In a discrete form, we have:

$$P_{m,n} = P_0 \cdot e^{-i \Delta k (m \sin \theta + n \cos \theta)}. \tag{B1}$$

Substitution of the discrete pressure field (eq. B1) in the staggered-grid wave eq. (eq. 24) gives the dispersion equation:

$$\begin{aligned}
\omega^2(k) &= \frac{v^2}{\Delta^2} [4\alpha_1\alpha_1 - 2\alpha_1\alpha_1 \cos(k\Delta \sin \theta) + 4\alpha_1\alpha_2 \cos(k\Delta \sin \theta) \\
&\quad - 4\alpha_1\alpha_2 \cos(2k\Delta \sin \theta) - 2\alpha_2\alpha_2 \cos(3k\Delta \sin \theta) \\
&\quad + 4\alpha_2\alpha_2 - 2\alpha_1\alpha_1 \cos(k\Delta \cos \theta) + 4\alpha_1\alpha_2 \cos(k\Delta \cos \theta) \\
&\quad - 4\alpha_1\alpha_2 \cos(2k\Delta \cos \theta) - 2\alpha_2\alpha_2 \cos(3k\Delta \cos \theta)]. \tag{B2}
\end{aligned}$$

We define the numerical phase and group velocities as $v_{\text{ph}} = \omega/k$ and $v_{\text{gr}} = \partial\omega/\partial k$ respectively. From eq. (B2) we get the relative numerical phase and group velocities:

$$\frac{v_{\text{ph}}^2}{v^2} = \frac{G^2}{4\pi^2} \left[4\alpha_1\alpha_1 \sin^2\left(\frac{\pi}{G} \sin\theta\right) + 8\alpha_1\alpha_2 \sin^2\left(\frac{\pi}{G} \sin\theta\right) - 8\alpha_1\alpha_2 \sin^2\left(2\frac{\pi}{G} \sin\theta\right) + 4\alpha_2\alpha_2 \sin^2\left(3\frac{\pi}{G} \sin\theta\right) \right. \\ \left. + 4\alpha_1\alpha_1 \sin^2\left(\frac{\pi}{G} \cos\theta\right) + 8\alpha_1\alpha_2 \sin^2\left(\frac{\pi}{G} \cos\theta\right) - 8\alpha_1\alpha_2 \sin^2\left(2\frac{\pi}{G} \cos\theta\right) + 4\alpha_2\alpha_2 \sin^2\left(3\frac{\pi}{G} \cos\theta\right) \right] \quad (\text{B3})$$

$$\frac{\partial\omega}{\partial k} = \frac{1}{2} \{ 2\alpha_1\alpha_1 [\sin\theta \sin(k\Delta \sin\theta) + \cos\theta \sin(k\Delta \cos\theta)] \\ + 4\alpha_1\alpha_2 [\sin\theta \sin(k\Delta \sin\theta) + \cos\theta \sin(k\Delta \cos\theta)] \\ - 8\alpha_1\alpha_2 [\sin\theta \sin(2k\Delta \sin\theta) + \cos\theta \sin(2k\Delta \cos\theta)] \\ + 6\alpha_2\alpha_2 [\sin\theta \sin(3k\Delta \sin\theta) + \cos\theta \sin(3k\Delta \cos\theta)] \} J^{-1/2}, \quad (\text{B4})$$

where $G = \lambda/\Delta = 2\pi/(k\Delta)$ denotes the number of grid points per wavelength λ and J is:

$$J = -2\alpha_1\alpha_1 [\cos(k\Delta \sin\theta) + \cos(k\Delta \cos\theta)] - 4\alpha_1\alpha_2 [\cos(k\Delta \sin\theta) + \cos(k\Delta \cos\theta)] \\ + 4\alpha_1\alpha_2 [\cos(2k\Delta \sin\theta) + \cos(2k\Delta \cos\theta)] - 2\alpha_2\alpha_2 [\cos(3k\Delta \sin\theta) + \cos(3k\Delta \cos\theta)] \\ + 4\alpha_1\alpha_1 + 4\alpha_2\alpha_2. \quad (\text{B5})$$

In order to illustrate the determination of accurate wave velocities by the staggered-grid approach we assume $\sin\theta \approx \theta$ for small angles θ and simplify the phase velocity dispersion relations (eqs B2 and B4):

$$\frac{v_{\text{ph}}}{v} = \alpha_1 - 3\alpha_2 \\ \frac{v_{\text{gr}}}{v} = \sqrt{\alpha_1\alpha_1 - 6\alpha_1\alpha_2 + 9\alpha_2\alpha_2}. \quad (\text{B6})$$

Using fourth-order staggered operator coefficients $\alpha_1 = 9/8$ and $\alpha_2 = -1/24$ (Levander 1988) we deduce, for both phase and group velocity, exactly 1.